IONIC CONDUCTIVITY IN RARE-EARTH DOPED

ALUMINOSILICATE GLASSES

By

MICHAEL RAY HOGSED

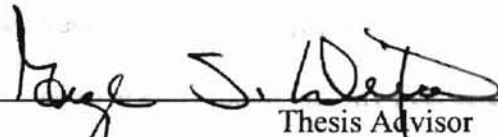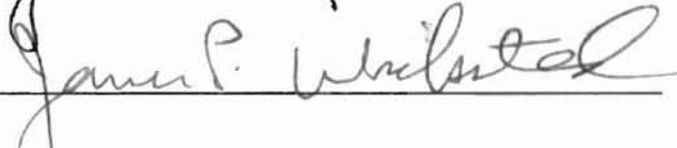Bachelor of Science

Baylor University

Waco, Texas

1997

Submitted to the Faculty of the
Graduate College of the
Oklahoma State University
In partial fulfillment of
The requirements for
The Degree of
MASTER OF SCIENCE
May, 1999

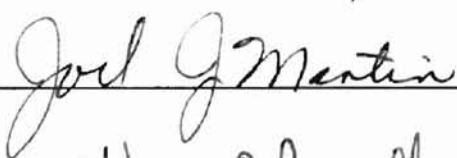# IONIC CONDUCTIVITY IN RARE-EARTH DOPED

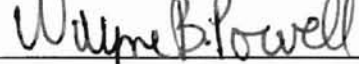# ALUMINOSILICATE GLASSES

Thesis Approved:

_____
Thesis Advisor

_____

_____

_____

_____
Dean of the Graduate College

ii

ACKNOWLEDGEMENTS

I would like to thank the members of my thesis committee, Dr. James Wicksted, Dr. Joel Martin, and Dr. David Peakheart for taking the time to thoughtfully evaluate this thesis. I am also grateful to Dr. Abdul Hamad and Mr. Charles Hunt for introducing me to the techniques of glass sample preparation. I am particularly indebted to my major advisor, Dr. George Dixon, who gave me the opportunity to do this work and was exceedingly patient with me all the way along.

My wife, Lori, has lovingly encouraged and supported me in my graduate work over these past two years. It is truly a joy and a privilege to be her husband.

Finally, I wish to acknowledge that my best efforts in life are ultimately worthless if they are not honoring to God. To Him be all glory and honor forever.

TABLE OF CONTENTS

LIST OF TABLES

LIST OF FIGURES

CHAPTER I

INTRODUCTION

A number of materials that are classified as electrical insulators can in fact conduct small electrical currents via transport of ions within the material. Glass has been known as such a material for over a century. Glass has long been valued for its utility as a workable transparent solid, and in recent years glass technology has flourished as the needs of the telecommunications industry for high speed networks have outgrown the utility afforded by copper wires. A recent development in optical communications is the creation of permanent laser-induced photorefractive index gratings in glasses. With the proper compositional make-up such glasses could one day be used for optical demultiplexers, narrow bandwidth notch filters, and read-only optical memories [5].

It has been found that the substitution of Al_2O_3 for some SiO_2 improves the efficiency of grating formation in one class of rare-earth doped glasses [25]. The process is also sensitive to the type of rare-earth dopant used. Induced long-range migration of network modifying ions, such as magnesium and sodium, is believed to be responsible for the formation of the photorefractive index gratings [28].

The purpose of this research is to investigate the compositional dependence of the ionic mobility in these glasses using conductivity measurements. In particular, the ionic conductivities of a family of europium doped sodium magnesium aluminosilicate glasses are measured as a function of Al_2O_3 concentration. Comparison will also be made between the effects of europium and praseodymium as rare-earth modifiers. In order to place these results in their proper context, some ionic conductivity theory will be

reviewed first. The structure of SiO_2 glass will be discussed briefly with the same intent. Also, an introduction to impedance spectroscopy will be given, along with a short review of the predominant impedance measurement techniques.

Ionic Conductivity

Ionic conductivity is the result of microscopic, thermally activated processes. The basic form of the temperature dependence found in ionic conductors can be shown by using a one-dimensional model which involves only one species of mobile ion in a periodic arrangement of potential wells (*e.g.* electronegative defect sites) [20]. Figure 1.1.a shows a cation trapped in one such potential well. The cation will oscillate with frequency, ν ($\approx 10^{13}$ Hz), inside the well. At a temperature, T, the probability that the oscillating ion will gain (from collisions with its neighbors) the energy, E_a, equal to that of the barrier, is $\exp(-E_a/kT)$ [3, 20]. The total number of hops made in a second will be $\nu \exp(-E_a/kT)$. Each direction is equally likely, so the net motion of the ion will be zero. If an electric field, ε, is applied in one direction, its effect will be the same as if the potential barrier on the right were lowered by $q\varepsilon d/2$ and the barrier on the left were raised by $q\varepsilon d/2$ as seen in figure 1.1.b [3,20]. Now, the net number of hops made per second in the preferential direction is given by

$$N_{hop} = \nu \exp[-(E_a - q\varepsilon d/2)/kT] - \nu \exp[-(E_a + q\varepsilon d/2)/kT]$$

$$= \nu \exp(-E_a/kT) [\exp(q\varepsilon d/2kT) - \exp(-q\varepsilon d/2kT)]$$

Figure 1.1.a – **Periodic potential wells**

$$d$$

Energy

$$E_a$$
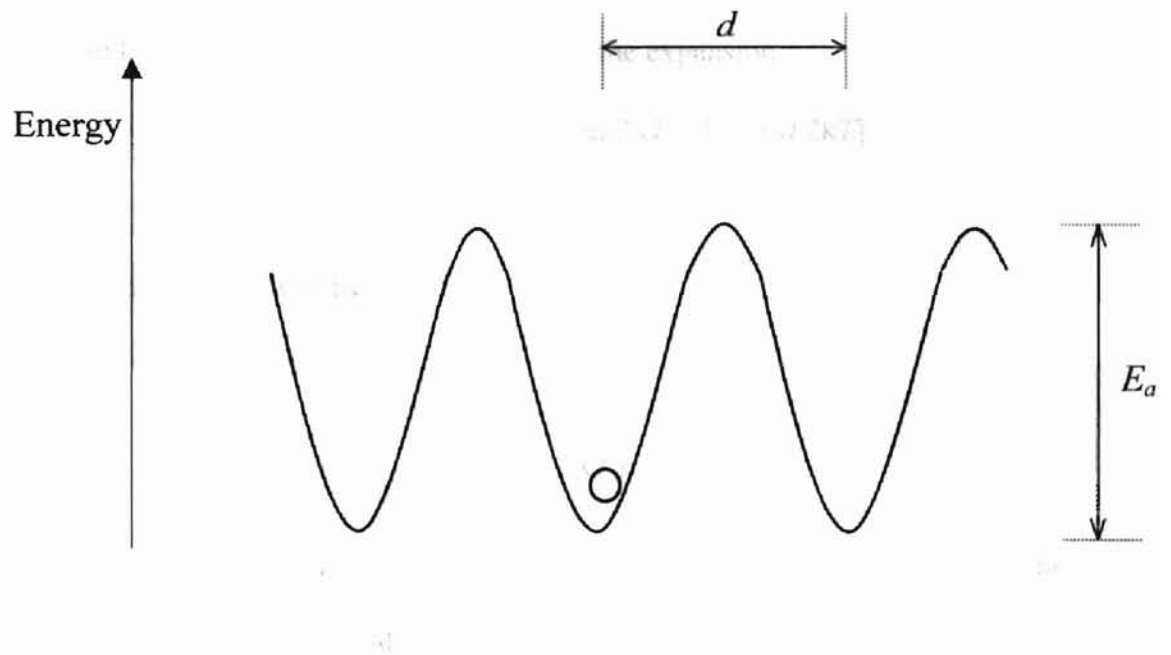
Figure 1.1.b – Periodic potential wells in the presence of an electric field

$$\varepsilon$$

Energy

$$E_a$$

$$q\varepsilon d/2$$

$$q\varepsilon d/2$$
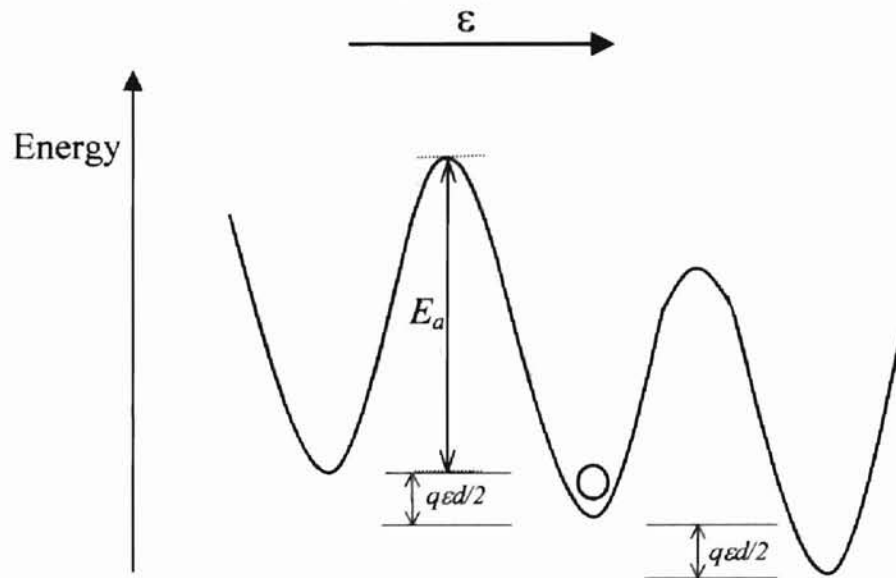
For the magnitude of electric field in common use for conductivity measurements, $q\varepsilon d$ is much smaller than $2kT$ [3,20], so the series expansion of the exponential is accurately approximated by the first two terms. Plugging in the expansion,

$$N_{hop} = v\exp(-E_a/kT)\ [1 + q\varepsilon d/2kT - 1 + q\varepsilon d/2kT]$$

$$= v\exp(-E_a/kT)[q\varepsilon d/kT] .$$

The current density is given by

$$J = nqdN_{hop}$$

$$= \frac{\varepsilon n v q^2 d^2}{kT}\exp(-E_a/kT)$$

where n is the number of these mobile cations per unit volume. The resistivity of the material, ρ, is the ratio of the applied electric field, ε, to the induced current density, J.

$$\rho = \frac{\varepsilon}{J}$$

$$= \frac{kT}{n v q^2 d^2}\exp\left(\frac{E_a}{kT}\right)$$

The conductivity, σ, is the inverse of the resistivity. So,

$$\sigma = \frac{1}{\rho} = \frac{n v q^2 d^2}{kT}\exp\left(-\frac{E_a}{kT}\right) ,\ \text{and}$$

$$\sigma T = \frac{n v q^2 d^2}{k}\exp\left(-\frac{E_a}{kT}\right)$$

$$= A\exp\left(-\frac{E_a}{kT}\right) .$$

A constant on the order of $1/3 - 1$ would also be included in the pre-exponential product in order to account for the number of ways the mobile ion can actually jump in a

three-dimensional crystal [20,26]. The expression above is called an Arrhenius equation. E_a is called the activation energy for ionic conduction. At a fixed temperature, its contribution to σ surpasses that of the pre-exponential factor, A. E_a , in the generally accepted terms of the Anderson-Stuart model, is the sum of two electrostatic energies which must be overcome for an ion hop [2]. The first of these, the binding energy, holds the ion in its equilibrium position. The second of these, the strain energy, is the energy associated with the required structural rearrangement in the immediate vicinity of the hopping ion [6]. The activation energy is temperature dependent, but over certain temperature ranges, it is nearly constant. In glasses, often one activation energy is operative from around 50 °C up to a point near the glass transition temperature [20].

If the electric field, ε, mentioned above, is varying in direction and magnitude as $\varepsilon_0 \exp(i\omega t)$, then the conductivity will be frequency (as well as temperature) dependent. AC conductivity in ionic conductors is larger than DC conductivity and is generally found to have a power law dependence [6] over a given frequency range of the type

$$\sigma_{ac} = \sigma_{dc} + B\omega^n$$

where $n \cong 1$. DC conduction involves the motion of ions over distances long in comparison to their size (e.g. the distance d in figure 1.1). If there were a number of smaller potential wells inside the large potential well, as in figure 1.2, the ion would have the thermal energy to overcome these barriers much more often than the barriers which are separated by the mean distance, d. The effect of a small DC field will be to once again decrease the large barrier on the right by $q\varepsilon d/2$ and raise the large barrier on the left by the same. Likewise, the small barrier on the right will decrease by $q\varepsilon a/2$ and the

Figure 1.2 – Hypothetical potential wells
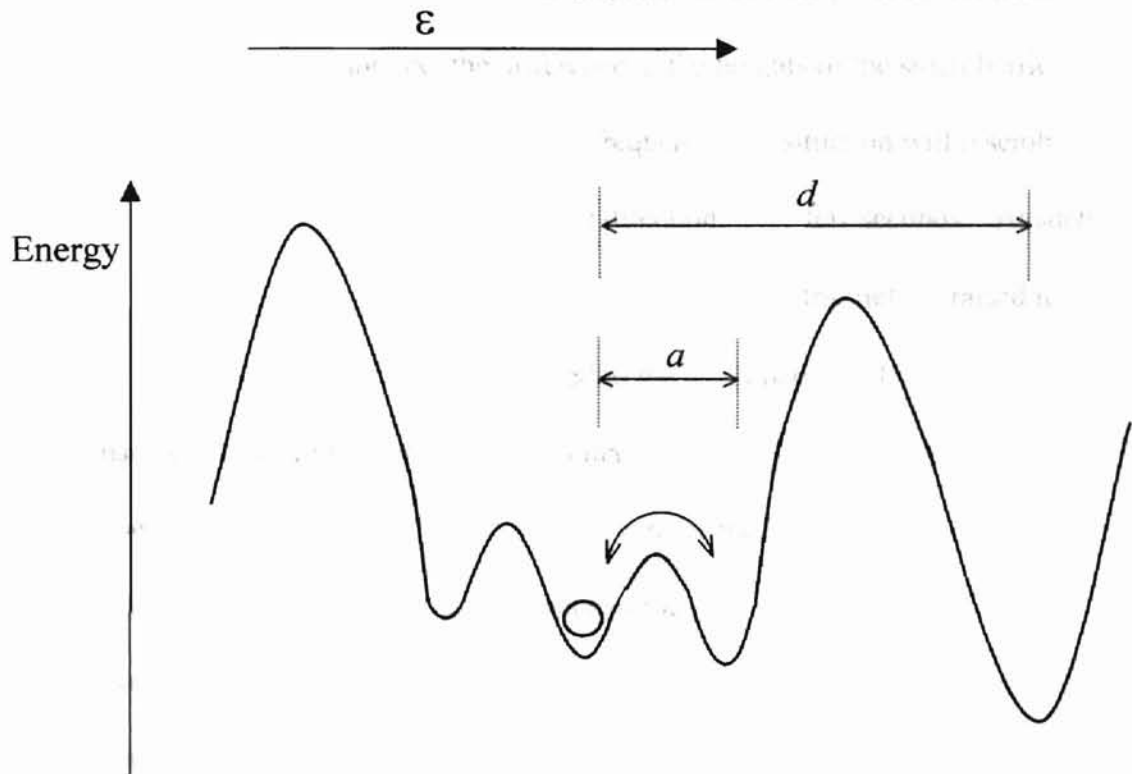
small barrier on the left will be raised by $q\varepsilon a/2$. The ion will quickly gain the thermal energy needed to hop over the first small barrier; however, it will take the same amount of time as before to gain the thermal energy needed to hop over the large barrier. That time is called the "relaxation time", τ_{dc}, of the long range conduction process. In that time, a very small electric field arising from the displacement of the positive ion from its negative center will tend to counteract the difference in the heights of the small barriers.

When a weak AC field is applied at a low frequency, the situation will resemble that of the DC field with the process alternating in direction every few seconds. At such a frequency, $\sigma_{ac} = \sigma_{dc}$. Suppose the angular frequency of the electric field is raised to approach the inverse of the relaxation time related to the small barriers, $1/\tau_{ac}$. In that case, the hops over the small barriers will have a maximum correspondence to the direction of the field, and they will contribute largely to the measured AC conductivity. In a random glass network, the height and distance of the potential barriers will be distributed around mean values. Hence, there is a distribution of relaxation times that significantly contribute to the AC conductivity over a large frequency range [20].

When placed in a DC electric field, an ionic conductor will exhibit some degree of instantaneous polarization, P_∞, corresponding to a shift of the electronic charge density relative to the nuclei [4]. The material will polarize further with time to a static level, P_s, as the partially mobile cations (those contributing to σ_{ac} in the above model) are displaced in the direction of the field. If the rise from P_∞ to P_s is exponential, then the total, time dependent polarization is

$$P(t) = (P_s - P_\infty)(1 - \exp(t/\tau)) + P_\infty$$

where the time constant for this process, τ, would correspond to the time required for an ion to gain the energy needed to hop over the small potential barriers in Figure 1.2. The relationship between the magnitude of the applied field (which will now be called E) to the magnitude of the resulting polarization in the particular material is given by

$$P = ((\varepsilon-1)/4\pi)E$$

where ε is called the dielectric constant. Suppose that this material is placed between two parallel planar electrodes, and that an alternating potential difference between the two electrodes, $V_0 \exp(i\omega t)$, is maintained. The charge density on the electrodes is given by the magnitude of the electric displacement, D. Were the material a perfect dielectric, with instant polarization, the dielectric displacement would be related to the electric field between the two electrodes by

$$D = \varepsilon_0\varepsilon\, E$$

where the dielectric constant, ε, simply indicates the size of the constant of proportionality between the dielectric displacement and the electric field in the specific material. Since the polarization in ionic conductors is not instantaneous, as described above, there is a phase difference between the dielectric displacement and the electric field given by

$$D_0 \exp [i(\omega t-\delta)] = \varepsilon_0\varepsilon\, E_0 \exp(i\omega t).$$

From this,

$$\varepsilon_0\varepsilon = (D_0/E_0) \exp(-i\delta)$$
$$= (D_0/E_0)[\cos\delta - i \sin\delta] .$$

So, in actuality, the dielectric constant is a complex quantity. The notation used in this thesis for complex quantities such as the dielectric constant is given as

$$\varepsilon = \varepsilon' - i\varepsilon''.$$

The real part is related to the instantaneous polarization that is in-phase with the applied electric field, and the imaginary part (called the "dielectric loss") is related to the component of the dielectric displacement that takes place at a frequency which is 90° out-of-phase with the electric field. The negative sign is chosen by convention to indicate the direction of the 90° phase shift. This component of the dielectric displacement, which is 90° out-of-phase with the electric field, corresponds to a flow of current that is in-phase with the electric field. Therefore, any short range or long range migration of ions in the direction of the electric field contributes to the dielectric loss, ε''. The ratio of the imaginary to real part of the dielectric constant is given by

$$\varepsilon''/\varepsilon' = \sin\delta/\cos\delta$$

$$= \tan\delta.$$

This quantity, called the loss angle, is commonly used to characterize the dielectric response of an ionic conductor. Using the exponential time-dependent polarization mentioned above and the assumption of one relaxation time, Debeye showed that the frequency dependence of ε would be

$$\varepsilon' = \varepsilon_\infty + (\varepsilon_s - \varepsilon_\infty)\frac{1}{1+\omega^2\tau_{ac}^2}$$

$$\varepsilon'' = \sigma_{dc}/\omega\varepsilon_0 + (\varepsilon_s - \varepsilon_\infty)\frac{\omega\tau}{1+\omega^2\tau_{ac}^2},$$

Figure 1.3 – Debye (solid line) and non-Debye (dashed line) frequency response of dielectric constant and dielectric loss. (from ref. 22)
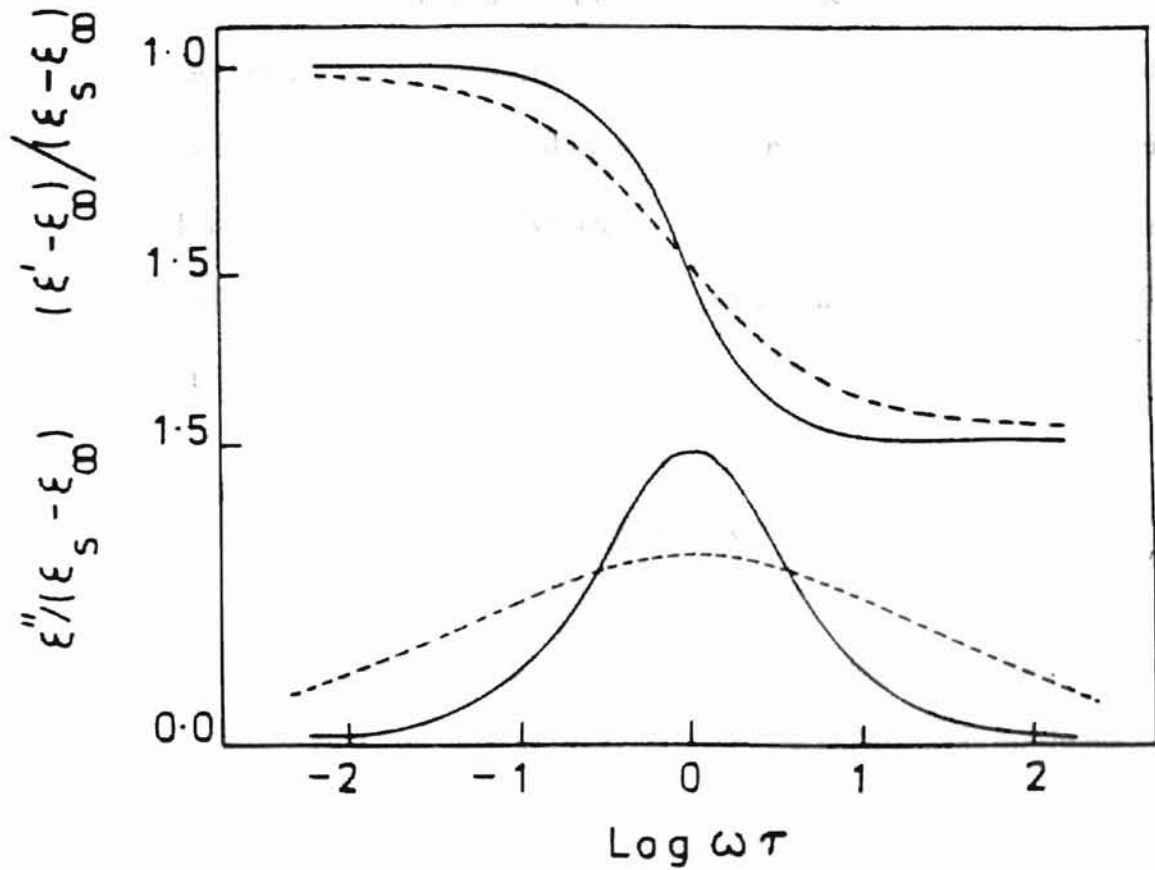
where ε_s is the real dielectric constant at $\omega = 0$, and ε_∞ is the real dielectric constant at optical frequencies. These functions are plotted in figure 1.3, along with an example of the dispersion that occurs with a symmetric distribution of relaxation times around τ_0.

While the dielectric relaxation (AC conductivity) behavior mentioned thus far is well established, the mechanism by which it occurs is still in question. The model of Stevels [20], which has been used here, is a reasonable choice based on the random structure of glass [8], but it has serious shortcomings. The average activation energy of the small peaks in figure 1.2 can be found by measuring the temperature dependence of the dielectric loss peak. It has been shown many times that the average activation energy of short range processes is approximately equal to the activation energy of long range DC conduction, contrary to what would be expected [8,3].

Silicate Glass Structure

The usual starting point for discussion about silicon dioxide glass structure is the set of rules put forward by Zachariasen in 1932 concerning the requirements for simple oxide glass formation [2]. These are as follows [2,24]:

1.) each oxygen atom is linked to no more than two cations

2.) the oxygen coordination number of the cation that forms the network is small

3.) oxygen polyhedra share only corners, and not edges or faces

4.) at least three corners of each polyhedra must be shared in order to form a three-dimensional network.

Three modifications of these rules for more complex glasses are as follows:

1.) the concentration of network forming cations which are surrounded by oxygen triangles or tetrahedra must be considerable

2.) the tetrahedra or triangles must be bonded at their vertices only

3.) certain oxygen atoms must be bonded to two such cations only; bonding to others is not possible.

These conditions, alone, do not distinguish oxide glass structures from many crystalline oxide structures. Zachariasen added that the long-range disordered characteristic of glass comes about from variations in bond angles, bond lengths, and rotation of the polyhedra about their axes [2].

When silicon is the network forming cation, the oxygen atoms bond tetrahedrally to make up the basic structural unit. The Si-O bond is partially ionic and partially covalent [24]. The Si-O-Si bond, which forms the bridge between two tetrahedra, varies in angle from 120 to 180° with a distribution maximum at 144°. Most of these angles are found to be within ± 10% of the distribution maximum [4]. The three-dimensional structure of SiO_2 is difficult to show pictorially, so a 2-dimensional schematic, such as figure 1.4, is often used to show a SiO_2 glass structure which makes use of the established ideas. In that figure, an oxygen atom is understood to be located above each silicon atom. Each oxygen atom in pure SiO_2 is expected to be a bridging oxygen, connecting two tetrahedra. Notice, that in the figure, rings of tetrahedra are formed with interstices that vary in size [2].

When an alkali oxide, such as Na_2O, is part of the glass composition, some of the bonds in the network break. This leaves electronegative non-bridging oxygens that are

Figure 1.4 – Schematic of SiO_2 glass network (after ref. 2)
An oxygen atom is understood to be located above each Si^{4+} cation.
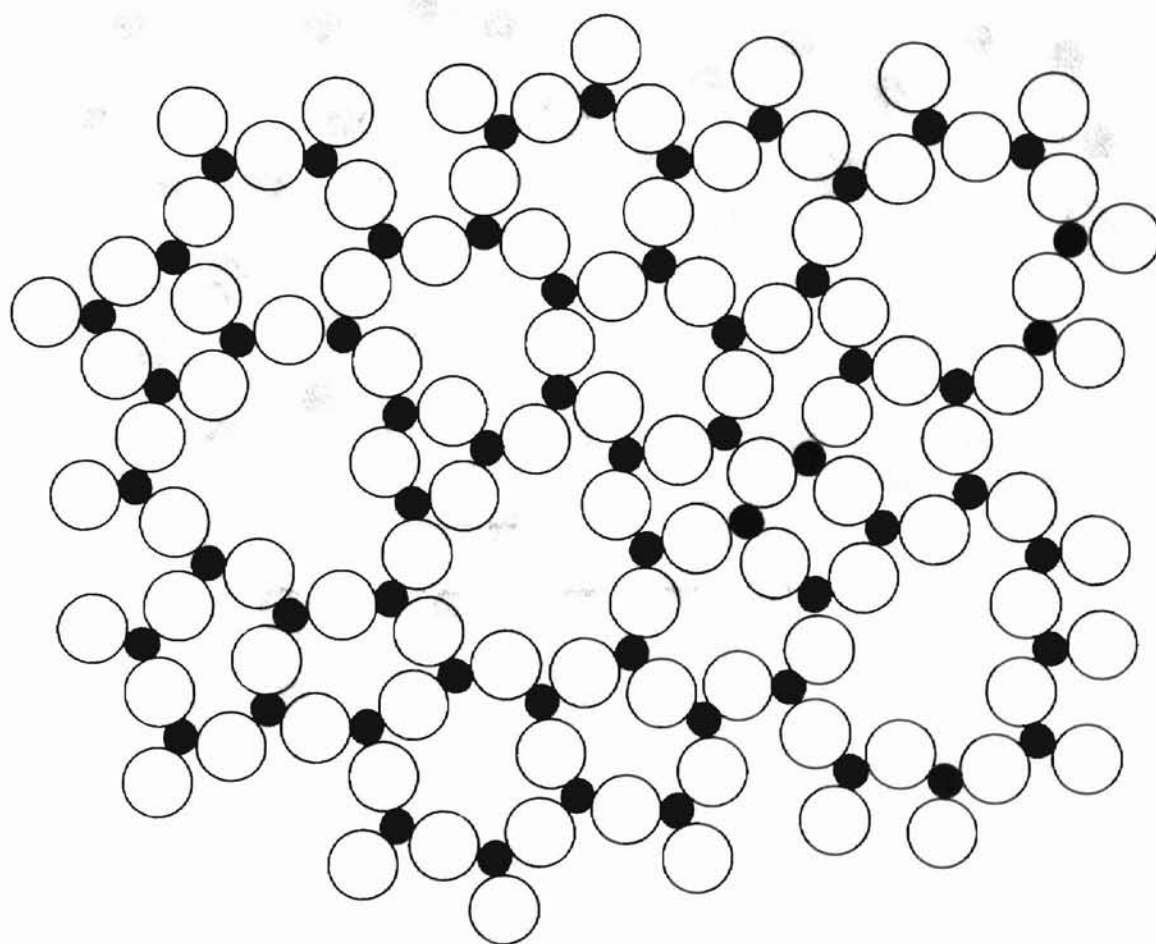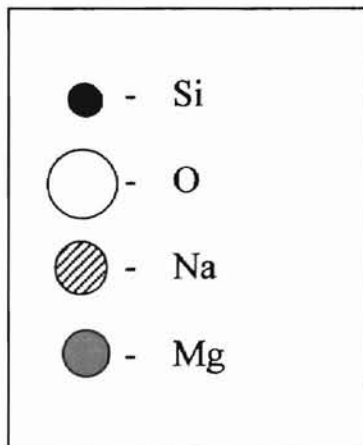
Figure 1.5 – Schematic of modified SiO_2 network (after ref. 2)
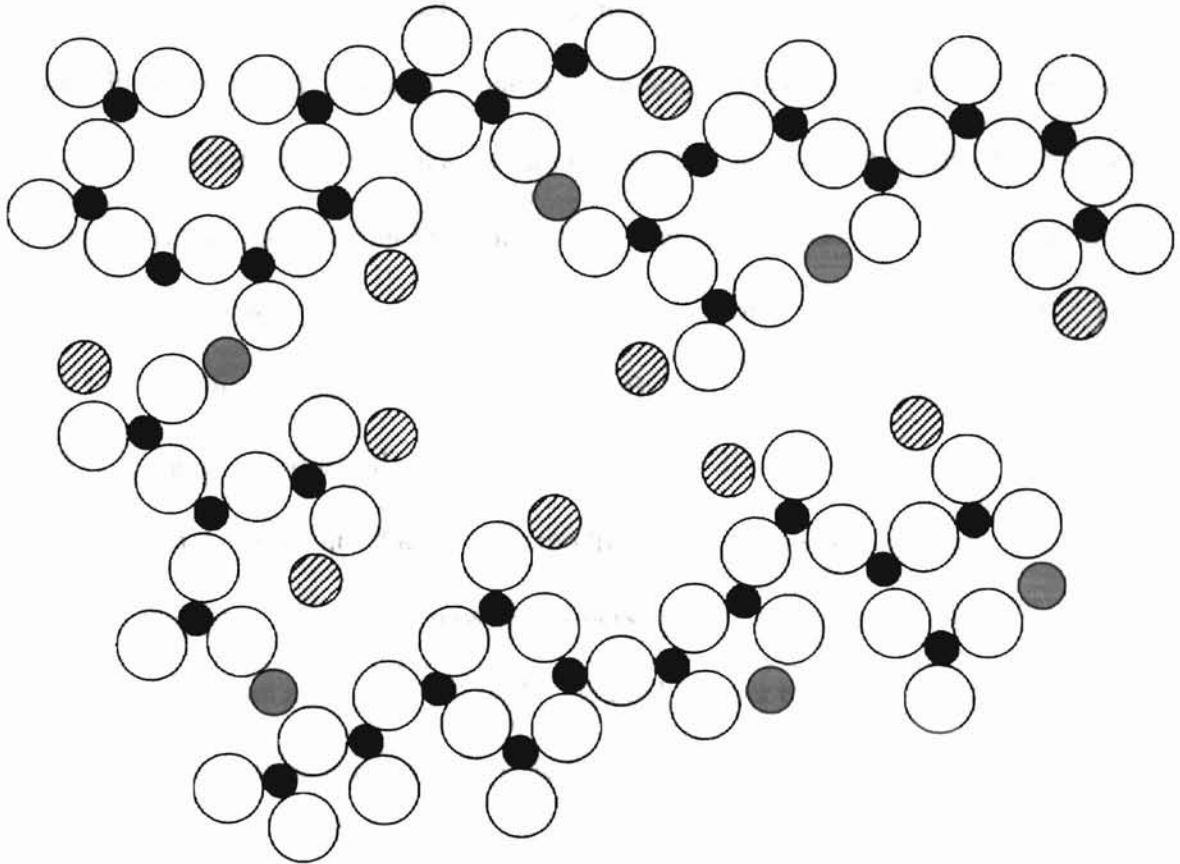
charge compensated by neighboring Na^+ ions. Alkaline-earth oxides, such as MgO, break up the network in the same way, but each Mg^{2+} ion will charge compensate twice as many non-bridging oxygens (NBOs). Elements, such as Na and Mg, that break up the network in this way are called network modifiers. A modified SiO_2 network schematic is shown in figure 1.5. For some calculations, it is useful to consider each alkali as being bonded to one NBO and each alkaline earth to two NBOs. EXAFS studies have shown, however, that the oxygen coordination number (including NBOs and BOs) of Na^+ in sodium silicate and sodium aluminosilicate glass is between five and eight [4,10]. The bond between the modifier and its associated NBO(s) is largely ionic, and therefore weaker and less directional than the partially covalent Si-O bonds [3].

When Al_2O_3 is introduced to the modified silicate glass composition, the Al^{3+} ions substitute for some Si^{4+} ions as network formers. There are 1.5 oxygen atoms introduced with each aluminum atom, rather than the required two per tetrahedron. Oxygen atoms which would otherwise become NBOs are therefore used to complete the AlO_4 tetrahedra. As the number of NBOs is decreased, the connectivity of the network increases. Each AlO_4 tetrahedron is charge compensated by a neighboring alkali ion. Likewise, two AlO_4 tetrahedra can be charge compensated by an alkaline-earth ion. The alkali-AlO_4 bond is weaker than the alkali-NBO bond, because the excess electron on the AlO_4 tetrahedron is less localized [11,12].

The average number of NBOs per tetrahedron can be quantified using Q_n notation [2]. Q_n represents a tetrahedron with n bridging oxygens. SiO_2 would consist of all Q_4 units since there are assumed to be no NBOs. It will be assumed that for each alkali modifier which is introduced, one Q_3 unit will replace one Q_4 unit. Likewise, for each

alkaline earth modifier, two Q_3 units will replace two Q_4 units. This will continue until each tetrahedron in the network has one NBO (*i.e.* all Q_3 units). After this, further introduction of modifiers will replace Q_3 units with Q_2 units, and so on. Using these assumptions, the method of quantization can be applied to the sodium magnesium aluminosilicate base of the glasses that are used in this study in order to estimate how the connectivity of the network changes with the addition of Al_2O_3. The composition of the undoped glass is $15Na_2O_3–xAl_2O_3–12MgO–(73-x)SiO_2$. The total number of tetrahedra per formula unit is

$$Q_3 + Q_4 = \overbrace{(73-x)}^{Si^{4+} cations} + \overbrace{2x}^{Al^{3+} cations} .$$

Also,

$$\overbrace{15 + 3x + 12 + (73-x)(2)}^{Total \# of oxygens} = Q_4 \overbrace{(2.0)}^{\substack{\# of oxygens \\ per Q_4 unit}} + Q_3 \overbrace{(2.5)}^{\substack{\# of oxygens \\ per Q_3 unit}}$$

$$15 + 3x + 12 + (73-x)(2) = \{2x + (73-x) - Q_3\}(2.0) + Q_3(2.5)$$

$$27 = x + (.5)Q_3$$

$$\Rightarrow \quad Q_3 = 54 - 2x .$$

The result shows that the network will return to total connectivity (*i.e.* no more NBOs) when the molar concentration of Al_2O_3 is 27%. The essence of the above method is that for each extra oxygen atom that is introduced along with a modifier, two NBOs will be created. Likewise, for each oxygen atom that is "taken" by a pair of network-forming aluminum cations, two NBOs will become bridging oxygens. It has recently been shown that rare-earth oxides act as network modifiers in this type of glass [29] , causing the number of NBOs to increase. However, when only 2.5 molar percent rare earth oxide is

added to 97.5 molar percent of the composition just considered, the calculated

concentration of NBOs changes very little.

Impedance Spectroscopy

Impedance spectroscopy is a relatively simple and non-destructive technique for

analyzing physical and chemical properties of a material [13]. The essence of the

technique is to observe the way in which the impedance of a material changes with

frequency. Doing so, one can discriminate between microscopic relaxation processes

[13], both in the bulk of the material and at the interfaces between the material and the

test device. The most elementary benefit that impedance spectroscopy offers is the

ability to separate the DC resistance of the electrode-material interface from the resistivity

of the material itself.

When an alternating potential difference $V_0 \, sin(\omega t)$ is applied across an ideal

resistive element, the output current is $I_r \, sin(\omega t)$. The same potential difference applied

across an ideal capacitor results in current $I_c \, sin(\omega t - \pi/2)$. In other words, the phase of

the alternating current is shifted by $90°$. An inductor responds by shifting the phase $90°$ in

the opposite direction. These responses can be plotted on a complex plane where the

vertical "imaginary" or "quadrature" axis corresponds to that part of I which is $90°$ out-

of-phase with V, and the horizontal "real" axis corresponds to that part of I which is

exactly in phase with V. Impedance, Z, is the ratio of the potential difference applied

across a circuit element or group of elements to the output current $Z = V/I$. In the case

of a resistor, $Z = Z' = R$. In the case of a capacitor, $Z = -iZ'' = -i(1/\omega C)$, so it is seen

that Z is, in general, a frequency dependent quantity. The impedance of any circuit composed of combinations of these two ideal elements can be derived by adding the impedances of any two elements in series with one another and adding the admittances $(Y = 1/Z)$ of any two elements in parallel with one another. An example is provided by a resistor and a capacitor in parallel such as is seen in figure 1.6.a. The admittance of this circuit is given by $Y = Y_R + Y_C = 1/Z_R + 1/Z_C = 1/R + i\omega C$. The impedance is then $Z = 1/(Y) = 1/(1/R + i\omega C)$ which is then rationalized to become

$$Z = \frac{1}{1/R + i\omega C} \times \frac{1/R - i\omega C}{1/R - i\omega C} = \frac{1/R - i\omega C}{1/R^2 + \omega^2 C^2} = \frac{R - i\omega R^2 C}{1 + (\omega RC)^2}.$$

It seen that in the low frequency limit, $Z \rightarrow R$, and in the high frequency limit, the imaginary component dominates as $Z \rightarrow 0$. The frequency dependent plot of this impedance in the complex plane is a semicircle, as seen in figure 1.6.b, which peaks at the frequency $\omega_0 = 1/(R_b C_\infty)$.

A very simple model of a conductor sandwiched between two blocking electrodes is an RC pair in series with a capacitance as seen in figure 1.7.a. In the figure, R_b is the bulk resistance of the sample, C_∞ is the capacitance of the cell, and C_{dl} is the "double layer" capacitance which accounts for the polarization that occurs at the electrode-bulk interfaces. The impedance of this circuit is

$$Z = \frac{R_b - i\omega R_b^2 C_\infty}{1 + (\omega R_b C_\infty)^2} - \frac{i}{\omega C_{dl}} = \frac{R_b}{(1 + (\omega R_b C_\infty)^2)} - i\frac{\left[1 + \omega^2 C_{dl} C_\infty R_b^2 + (\omega R_b C_\infty)^2\right]}{\omega C_{dl}\left[1 + (\omega R_b C_\infty)^2\right]}$$

In the low frequency limit, $Z' \rightarrow R_b$ and $Z'' \rightarrow \infty$; leading to the vertical spike on the low frequency end of figure 1.7.b.

Figure 1.6.a – RC pair circuit

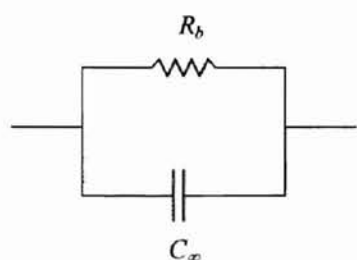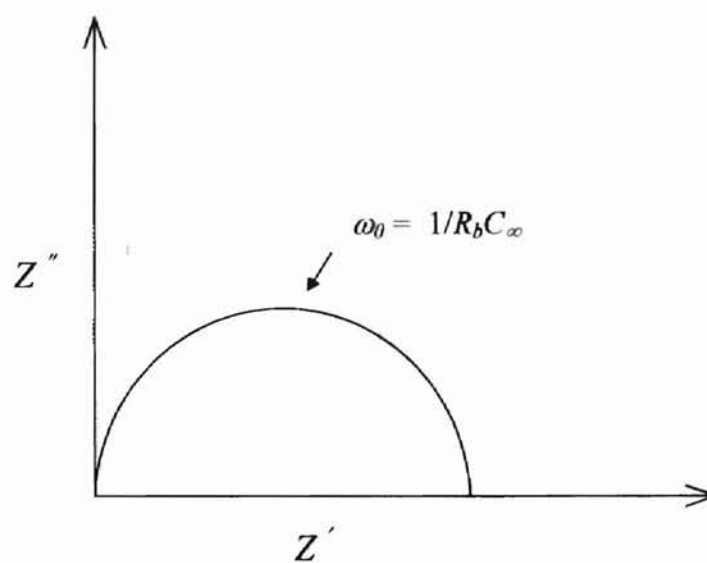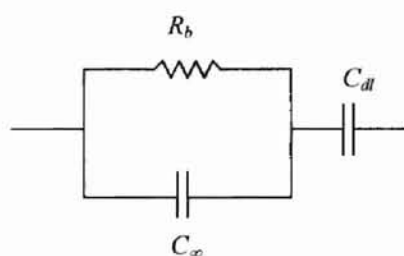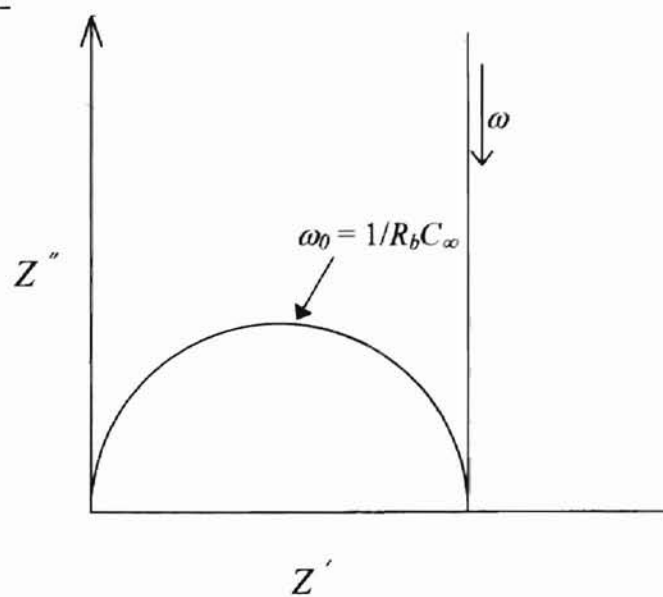Figure 1.6.b – Impedance plot of RC pair

$\omega_0 = 1/R_b C_\infty$

Figure 1.7.a – RC pair in series
with capacitor

Figure 1.7.b – Impedance plot of RC pair
in series with capacitor

$C_{dl} \gg C_\infty$

ω

$\omega_0 = 1/R_b C_\infty$

Ionic conductors never behave exactly as modeled in Figure 1.6.b. A flattened semicircle such as in figure 1.8 is one of the most common of the deviations from the ideal bulk response. The physical basis for this response is likely to be a distribution of relaxation times, which could be modeled by a long series combination of ideal RC pairs; each pair having different values of $\tau (= RC)$ [6]. Such a response can also be modeled by one resistor in parallel with a hypothetical circuit element called a constant phase element (CPE). The admittance of a CPE is $Y = 1/Z = A_0(i\omega)^\psi$, with $0 \leq \psi \leq 1$. For ψ = 1 this would simply be the response of a capacitor (with $A_0 = C$). Another place where CPE behavior can be observed is at the interface between the blocking electrode and the material. In this case, the basis for the CPE behavior is thought to be the microscopic roughness of the electrode and the resulting variation in the distance of closest approach by the neighboring mobile ions [17].

The data gained from impedance spectroscopy can be used to determine the frequency dependent, complex dielectric constant, ε, which was mentioned previously. The measured electric current is given by the time derivative of the charge (or equivalently, D) on the electrodes [8,1],

$$I = (dD/dt)A$$

$$= [d(\varepsilon_0\varepsilon \, E_0\exp(i\omega t))/dt]A$$

$$= i\omega \, A \, \varepsilon_0\varepsilon \, E_0 \exp(i\omega t)$$

$$= E \, A \, i\omega \, \varepsilon_0\varepsilon$$

$$= (V/l)A[i\omega\varepsilon_0(\varepsilon' - i\varepsilon'')]$$

$$= (V/l)A[\omega\varepsilon_0(i\varepsilon' + \varepsilon'')]$$

Figure 1.8 – CPE in parallel with resistor
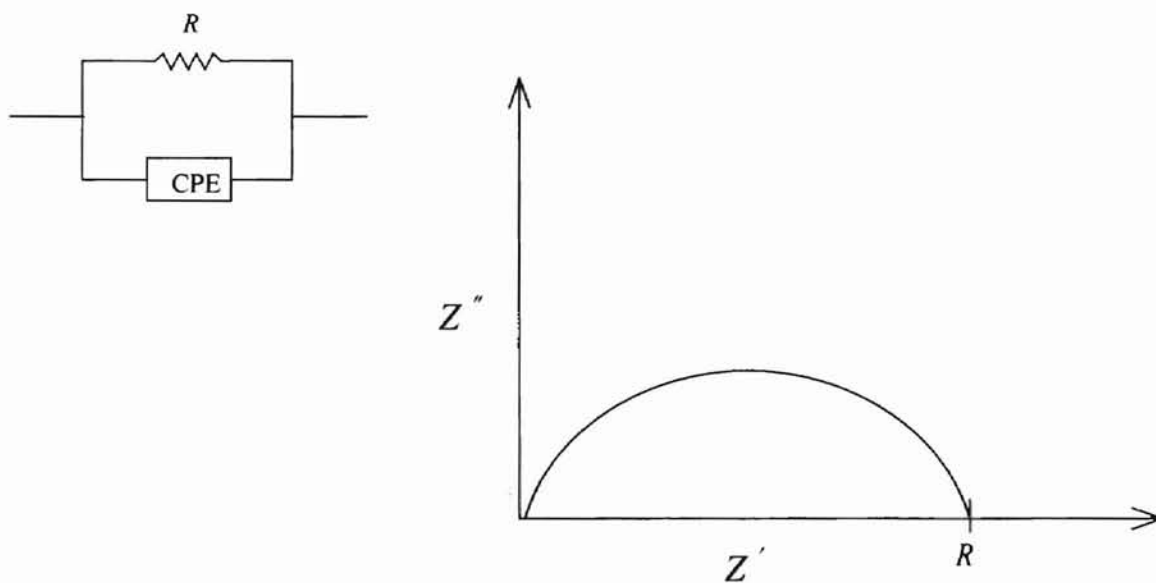
$Y_{circuit} = 1/R + iA\omega^n$

$$Z_{circuit} = \frac{R}{1 + iRA\omega^n} \times \frac{1 - iRA\omega^n}{1 - iRA\omega^n}$$

$$= \frac{R - iR^2 A\omega^n}{1 + R^2 A^2 \omega^{2n}}$$

Using the relation $Z = 1/Y = V/I$, it is seen that

$$Y = (A/l)[\omega\varepsilon_0(i\varepsilon' + \varepsilon'')] \,,$$

which is can also be written as

$$\frac{Z' + iZ''}{Z'^2 + Z''^2} = \omega C_\infty [i\varepsilon' + \varepsilon'']$$

$$\Rightarrow \qquad \varepsilon' = \frac{1}{\omega C_\infty} \frac{Z''}{Z'^2 + Z''^2}$$

$$\varepsilon'' = \frac{1}{\omega C_\infty} \frac{Z'}{Z'^2 + Z''^2} \,.$$

Recall that part of the dielectric loss is due to the long range DC conductivity. The amount that this loss contributes is $\sigma_{dc}/\omega\varepsilon_0$. If the dielectric loss due to the short range polarization of ions is the desired quantity, then $\sigma_{dc}/\omega\varepsilon_0$ must be subtracted from ε'' at each frequency.

The electric modulus, defined by $M = 1/\varepsilon$, is a function which has also been used in recent years to display frequency dependent dielectric responses. The real and imaginary components are given by

$$M = \frac{1}{\varepsilon' - i\varepsilon''} \times \frac{\varepsilon' + i\varepsilon''}{\varepsilon' + i\varepsilon''}$$

$$= \frac{\varepsilon' + i\varepsilon''}{\varepsilon'^2 + \varepsilon''^2}$$

The imaginary component of the electric modulus exhibits a peak when plotted as a function of frequency [1,8]. This is especially helpful when the dielectric behavior of the

material is obscured at low frequencies by DC conductivity and polarization at the electrode/material interface [8]. For example, ε'' is supposed to display a peak at a frequency that is equal to the inverse of the mean relaxation time, τ_{ac}. However, the low frequency side of the peak will also contain the σ_{dc} contribution. The lower the frequency, the larger this contribution will be, and subtracting it may limit the precision of the data too much. The imaginary component of the modulus goes to zero as the dielectric loss becomes very large, so a modulus peak can be distinguished from the same impedance data that would not display a dielectric loss peak. The modulus peak occurs at a higher frequency, so the mean relaxation time that is derived from the modulus will not be equal to the mean relaxation time derived from the dielectric constant [18]. However, the two are proportional to one another, with the proportionality being determined by the functional form of the distribution of relaxation times [18].

Experimental Techniques

There are a large number of AC frequency response techniques that can be used for impedance spectroscopy. These techniques may be categorized broadly as comparison techniques and direct measurement techniques [1,14]. AC bridges are the instruments used in the first category. Lock-in amplifiers and frequency response analyzers will be discussed as two worthwhile examples of the second category [1,16].

AC bridges are variations on the basic principle of the Wheatstone bridge shown in figure 1.9. The impedances Z_1, Z_2, and Z_3 are known, variable circuit elements. Through an iterative process of changing the variable circuit elements, the condition is

Figure 1.9 – Basic Wheatstone bridge
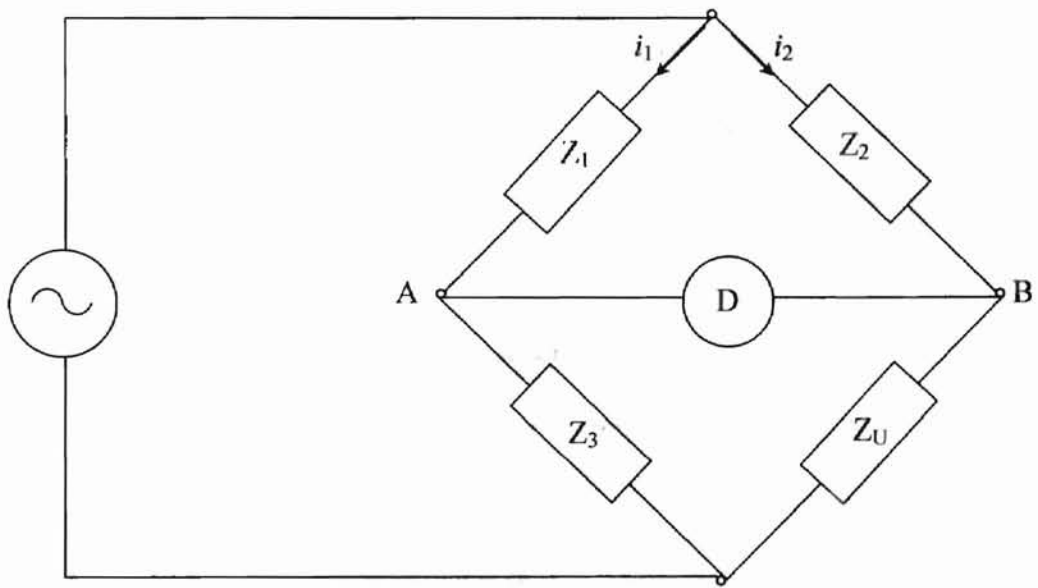
created where the potential at A is equal to the potential at B, or equivalently $i_1 Z_1 = i_2 Z_2$

and $i_1 Z_3 = i_2 Z_U$ [7]. Hence, $\dfrac{i_1 Z_1}{i_1 Z_3} = \dfrac{i_2 Z_2}{i_2 Z_U} \Rightarrow Z_U = \dfrac{Z_2 Z_3}{Z_1}$. The ratio arms containing

Z_2 and Z_1 are included to scale the impedance of Z_U into the range of Z_3 if needed.

Limitations on high frequency measurements are imposed by the non-ideal nature

of the reference circuit elements and stray capacitances [1,21]. Low frequency bridge

measurements are often limited by noise sources that are amplified at the null detector

[1]. The high frequency limitations have been largely overcome by bridge devices that

use transformers as ratio arms. In fact, separate bridge methods have been devised to

probe into the extremes of the high frequency range ($>10^6$ Hz) and the low frequency

range ($<10^{-3}$ Hz), however, no single bridge method can reliably cover both. A number of

the devices that can be used to improve the accuracy of the bridge results (phase sensitive

detectors; filters, ADCs, etc.) will be discussed in terms of their use in direct

measurement devices. One more drawback of bridge devices is that most of them are

not automated, and therefore require greater skill and time from the operator. Collection

of impedance data over many different frequencies usually can not be done quickly

enough for application of impedance spectroscopy to systems which are changing with

time [1]. Quality automated bridges have been produced in recent years [4,21], but the

added complexity counteracts the low costs normally associated with AC bridges.

The goal of direct impedance measurement instruments is to analyze the way in

which a signal has been modulated after passing through a test sample. A lock-in

amplifier is such an instrument designed to distinguish the magnitude and phase of very

small AC signals, even when those signals are obscured by noise sources many times

larger than the signals themselves [15]. The key components in the accomplishment of this task are the phase sensitive detectors (PSDs).

A phase sensitive detector (or multiplier) works in tandem with a low pass filter (or time averaging circuit) in order to separate a signal with a precise phase and frequency from other signals. The phase sensitive detector multiplies the input sine wave V_i $\sin(\omega_i t + \phi)$ with a reference sine wave $V_r \sin(\omega_r t)$ to get an output

$$V_{psd} = \frac{1}{const.}\left\{\frac{1}{2}V_i V_r \cos[(\omega_r - \omega_r)t - \phi] - \frac{1}{2}V_i V_r \cos[(\omega_r + \omega_i)t + \phi]\right\}$$

$$= \frac{1}{2}BV_r \cos(\phi) - \frac{1}{2}BV_r[2\omega t + \phi].$$

where B is a dimensionless constant that takes into account the amplitude contribution of the reference signal. When this signal is time averaged, it becomes

$V_{psd} = \frac{1}{2}BV_r \cos(\phi)$; a DC output that is proportional to that part of the input signal

which is in phase with the reference signal [15]. If the input signal is a mix of waves at various frequencies, which is the usual case, only the PSD output term corresponding to the waves with frequency ω_r will not time average to zero, so the PSD is frequency selective [1,9]. A separate phase sensitive detector multiplies with a reference signal that is shifted by 90° in order to display the component of the input signal that is exactly out-of-phase with the original reference signal.

Figure 1.10 is a functional diagram of the lock-in amplifier chosen for the present research - the Stanford Research Systems SR830 DSP. Optional functions that were not used in this research are not included in the figure. An internal oscillator generates a

Figure 1.10 – SRS 830 DSP lock-in amplifier (after ref. 15)
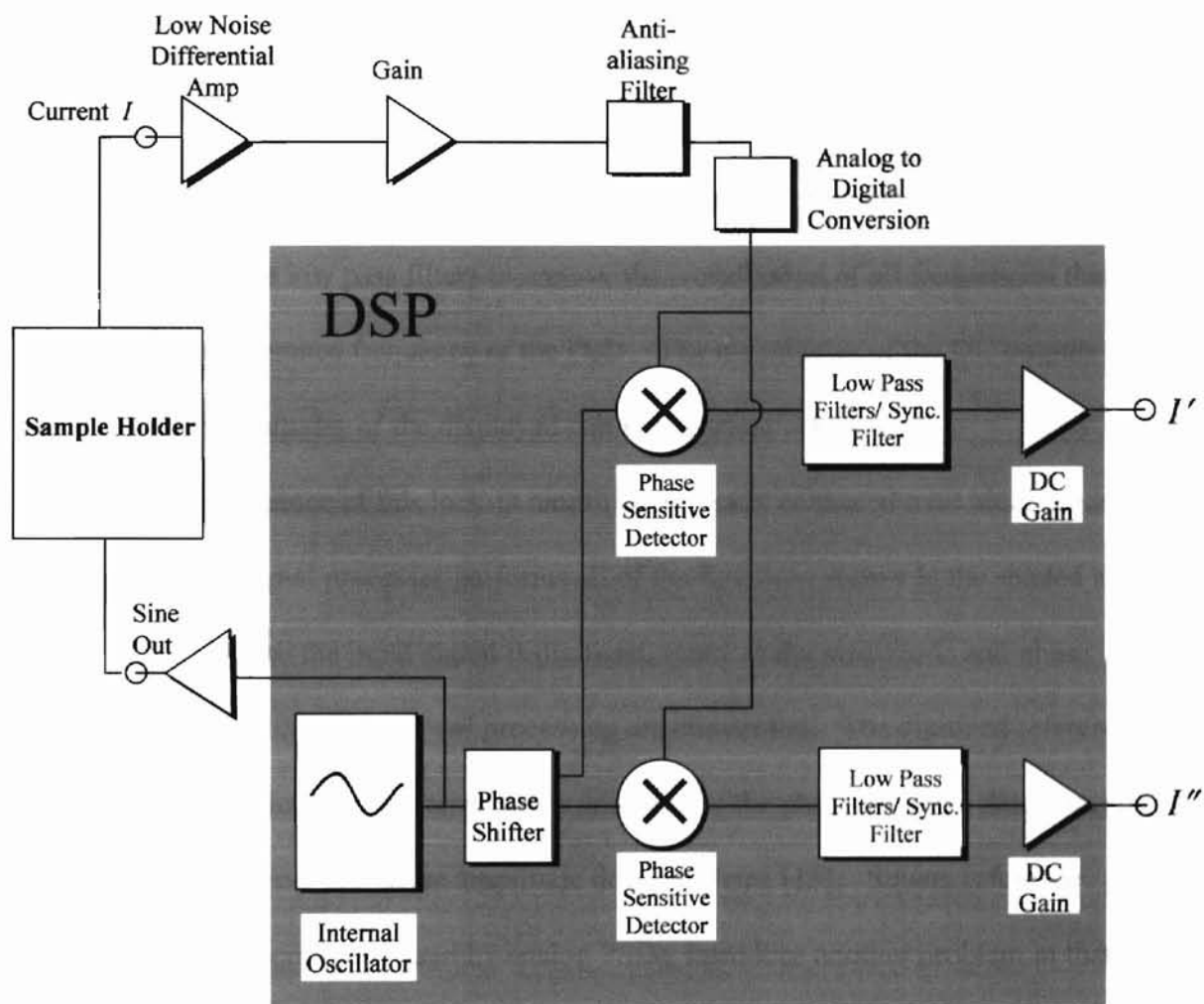
digitally synthesized sinusoidal reference wave from which a sinusoidal voltage output of desired amplitude is produced. This desired potential difference between the output and the current input (connected in series to a virtual ground) is actively maintained. The input current is converted to an analog voltage signal and passed through an anti-aliasing filter, which sharply attenuates analog signals with frequencies higher than 102 kHz. The analog signal is amplified and converted to a digital signal. That signal passes through two phase sensitive detectors in parallel. The AC output of each PSD is then time averaged in the low pass filters to remove the contribution of all frequencies that are not equal to the reference frequency of the PSD. The magnitudes of the DC outputs determine the magnitudes of the displayed complex current components.

The performance of this lock-in amplifier is greatly enhanced over older models because a digital signal processor performs all of the functions shown in the shaded area of figure 1.10. Once the input signal is digitized, many of the magnitude and phase errors associated with analog signal processing are eliminated. The digitized reference sine wave is of particular importance to the accuracy of the phase sensitive detectors since analog sine wave generators have amplitude drift problems [15]. Square reference signals, which are commonly used by analog PSDs, introduce another problem in that odd order harmonics of the reference frequency do not time average to zero after being multiplied with a square reference signal [1,9]. Although the detection of current has been discussed, a lock-in amplifier can alternatively be configured to detect a voltage drop across the sample. This configuration is recommended for a sample impedance less than 10^6 Ω because capacitive coupling noise current generates very little voltage [15]. The operating frequency range of the SRS 830 DSP lock-in amplifier is 10^{-3} to 10^5 Hz.

This makes it suitable for impedance measurements on material with a conductivity of about 10^{-9} to 10^{-6} $\Omega^{-1}cm^{-1}$. Direct measurements on materials outside of this conductivity range are best made with frequency response analyzers.

Frequency response analyzers (FRAs) are automated devices designed specifically for the direct measurement and display of impedance over a wide frequency range. Figure 1.11 shows a schematic of a basic FRA. In the simplest type of voltage divider operation, an alternating signal $A_0 \sin(\omega_r t)$ can be applied to the sample in series with a standard impedance. A voltage $V(t)$ is detected at two different points in the experimental circuit. One FRA input measures the potential drop across the standard resistor and the other measures the potential drop across the series combination of the sample and the resistor. Each signal is separately digitized and analyzed in the same way, so the operation of a single analyzer will now be described. As with the lock-in amplifier, $V(t)$ is multiplied by the in-phase and out-of-phase components of the digitally generated reference signal $V_r \sin(\omega_r t)$ and $V_r \cos(\omega_r t)$. The "multipliers" are essentially the same devices as the PSDs already discussed, but they are not referred to by that name in order to distinguish that the time-averaging of the output is accomplished by digitally integrating over an integral number of cycles. The output of the multipliers is $V(t)\sin(\omega_r t)$ and $V(t)\cos(\omega_r t)$, where

$$V(t) = BA_0 |Z(\omega_r)| \sin(\omega_r t + \phi) + \text{harmonic terms} + \text{noise terms}.$$

$Z(\omega_r)$, in this general case, is the transfer function which relates the stimulating sine wave, $A_0 \sin(\omega_r t)$, to the response measured at a point in the experimental circuit. The multiplier outputs are then integrated as follows [1,10]:

Figure 1.11 – Voltage divider operation of FRA
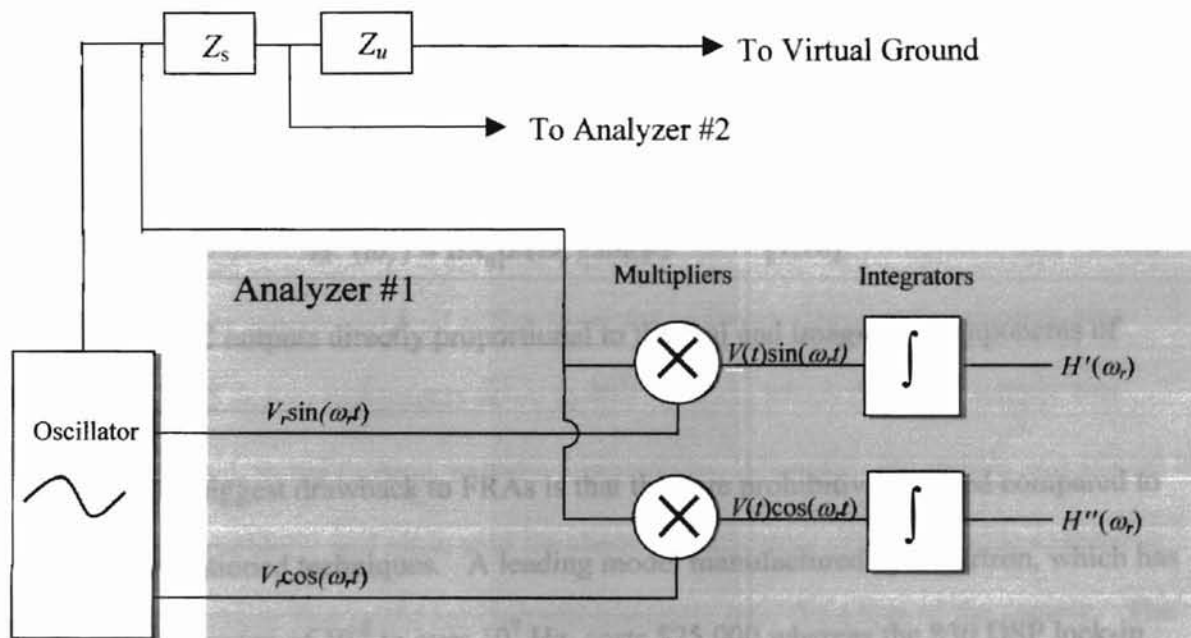
$$H'(\omega_r) = \frac{1}{T} \int_0^T V(t) \sin(\omega_r t) \, dt$$

$$H''(\omega_r) = \frac{1}{T} \int_0^T V(t) \cos(\omega_r t) \, dt \quad .$$

The harmonic terms that are part of $V(t)$ will integrate to zero as long as the integration is performed over an interval of time, T, equal to an integral number of cycles. The noise terms will integrate to zero over large T. The output of the integrators is then

$$H'(\omega_r) = BA_0 |Z(\omega_r)| \cos(\phi)$$

$$H''(\omega_r) = BA_0 |Z(\omega_r)| \sin(\phi) \qquad [1,10]$$

which are DC outputs directly proportional to the real and imaginary components of impedance.

The biggest drawback to FRAs is that they are prohibitively priced compared to the aforementioned techniques. A leading model manufactured by Solartron, which has an operating range of 10^{-5} to over 10^7 Hz, costs \$25,000 whereas the 830 DSP lock-in costs \$6,000. Often, a separate impedance adapter must also be purchased, as well as operating software. Even a FRA that only covers a frequency range comparable to the digital lock-in costs twice as much. The greater expense can be attributed to superior frequency selectivity, the inclusion of more than one analyzer of the type shown in Figure 1.11 (allowing for three electrode configurations), automated nulling functions to subtract apparatus contributions, and automated display of impedance related functions.

CHAPTER II

EXPERIMENT

Sample Preparation

All of the samples, with the exception of sample B1, were made in the OSU crystal growth lab. Each glass sample was cut to be less than or equal to 1mm in thickness. The parallel planar surfaces were fine polished with cerium oxide. Each sample was annealed at 550 $^{\circ}$C for about 15 hours and then cooled down to 525 $^{\circ}$C at a rate of 2 $^{\circ}$C per minute and held at that point for an hour. This cooling process was repeated in 25 degree increments down to 400 $^{\circ}$C, from which point the sample was allowed to cool, in the furnace, to room temperature. After that, the sample was placed in a mix of hydrochloric and nitric acid for about two minutes. This was done to remove any metallic traces that might conduct electronically over the edges of the sample. The faces of the sample were then fine polished again. The sample was cleaned ultrasonically in de-ionized water, and placed in a furnace for 45 minutes at 150 $^{\circ}$C in order to bake off surface moisture. A thin layer of AuPd was then sputtered on to a circular area of each face of the sample, creating parallel plane electrodes. The composition of each sample is listed in Table I, along with the length and area measurements of the plated surfaces.

Table I – Sample compositions

Component	A1	A2	A3	A4	A5	B1	B2	B3
SiO_2	73	70	67	64	58	70	70	64
Al_2O_3	0	3	6	9	15	3	3	9
MgO	12	12	12	12	12	12	12	12
Na_2O	15	15	15	15	15	15	15	15
Eu_2O_3	2.5	2.5	2.5	2.5	2.5	-	-	-
Pr_2O_3	-	-	-	-	-	2.5	0.5	0.5

* Base composition without rare earth

Table II – Sample dimensions

Sample	Thickness	Area	l/A ($\pm$ 3%)
A1	1.03 mm	123 mm^2	0.0837 cm^{-1}
A2	1.05 mm	123 mm^2	0.0854 cm^{-1}
A3	0.669 mm	120 mm^2	0.0558 cm^{-1}
A4	0.527 mm	119 mm^2	0.0554 cm^{-1}
A5	0.810 mm	37.0 mm^2	0.219 cm^{-1}
B1	0.669 mm	95.2 mm^2	0.0703 cm^{-1}
B2	0.675 mm	121 mm^2	0.0558 cm^{-1}
B3	0.693 mm	125 mm^2	0.0554 cm^{-1}

Figure 2.1 – Sample holder

½ in.

AC lead

Heating Coil

Grounded shield

AC lead

Thermocouple Tube

Grounded Shield
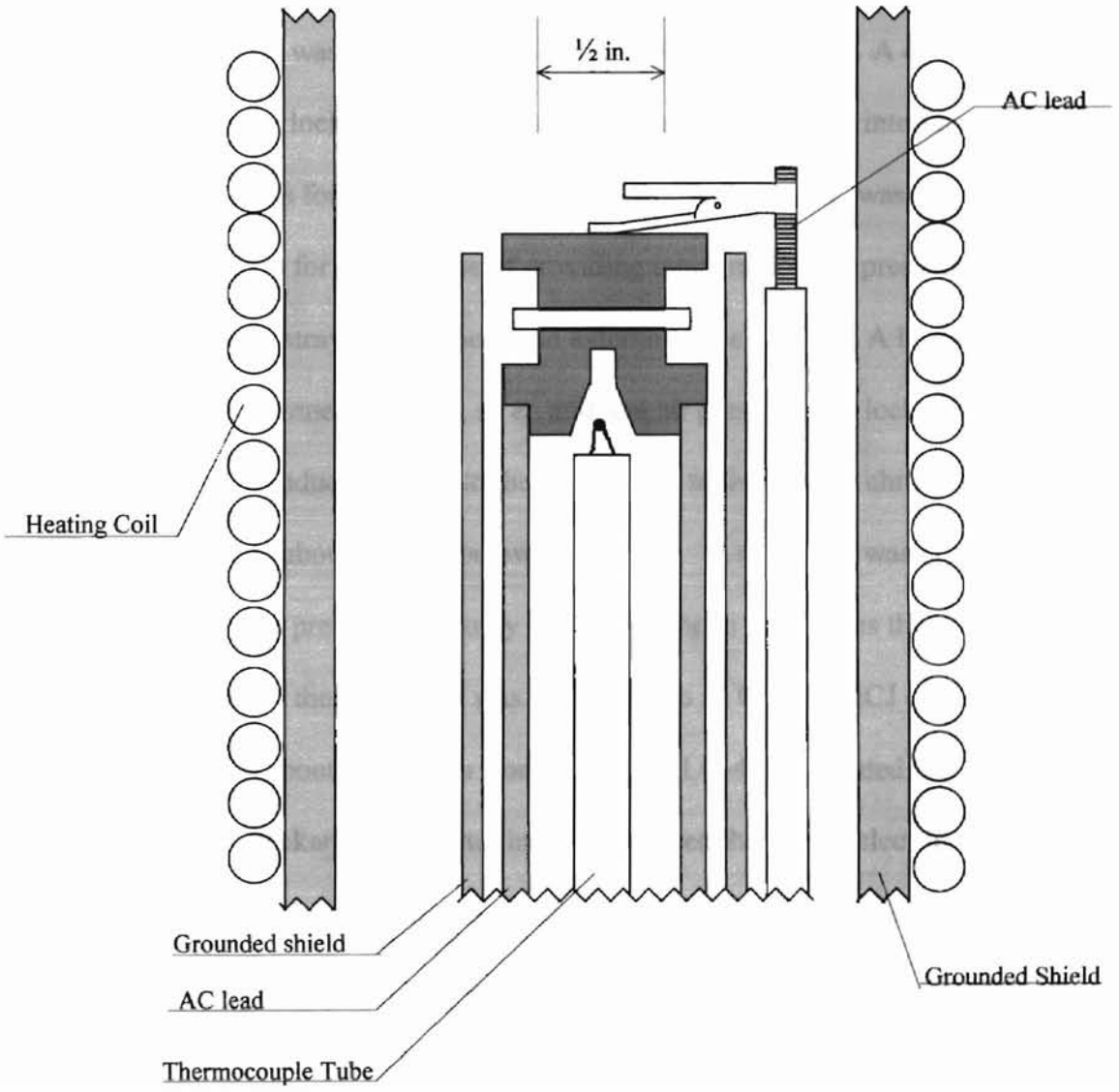
Experimental Setup

The sine wave generator of the model 830 DSP (Digital Signal Processor) lock-in amplifier was used to maintain an AC potential difference of 0.026 Volts (rms) across the sample. The frequency range of the lock-in is 10^{-3} to 10^5 Hz, however, the useful range for these glass samples was found to be limited to .5 Hz - 20,000 Hz. A data collection program controlled the lock-in operation remotely over an IEEE-488 interface. The stainless steel apparatus for holding the sample, shown in figure 2.1, was constructed in the OSU machine shop for the purpose of providing temperature and pressure control, as well as shielding from stray capacitances and external noise sources. A heating coil was located external to the inner chamber, so an ambient air pressure was locked in to the chamber in order to conduct the heat to the sample and to the interior chromel-alumel thermocouple, located about an inch below the sample. A slow leak was allowed in order to ensure that the pressure rose only minimally above ambient as the temperature increased. The interior thermocouple was referenced to an Omega MCJ electronic ice point which received about 1.35 Volts from a Lambda LQ-413 regulated DC power supply. A Hewlett Packard 3478A multimeter displayed the thermoelectric voltage of the interior thermocouple with a random fluctuation of ± 0.001 mV, which corresponded to fluctuations in the temperature measurement of about ± 0.025 degrees; a negligible quantity. An Omega CN-2000 temperature controller, with an internal electronic ice point, was connected to the heating coil and to a thermocouple located near the coil. A diagram of the described experimental setup is shown in figure 2.2.

Figure 2.2 – Experimental setup
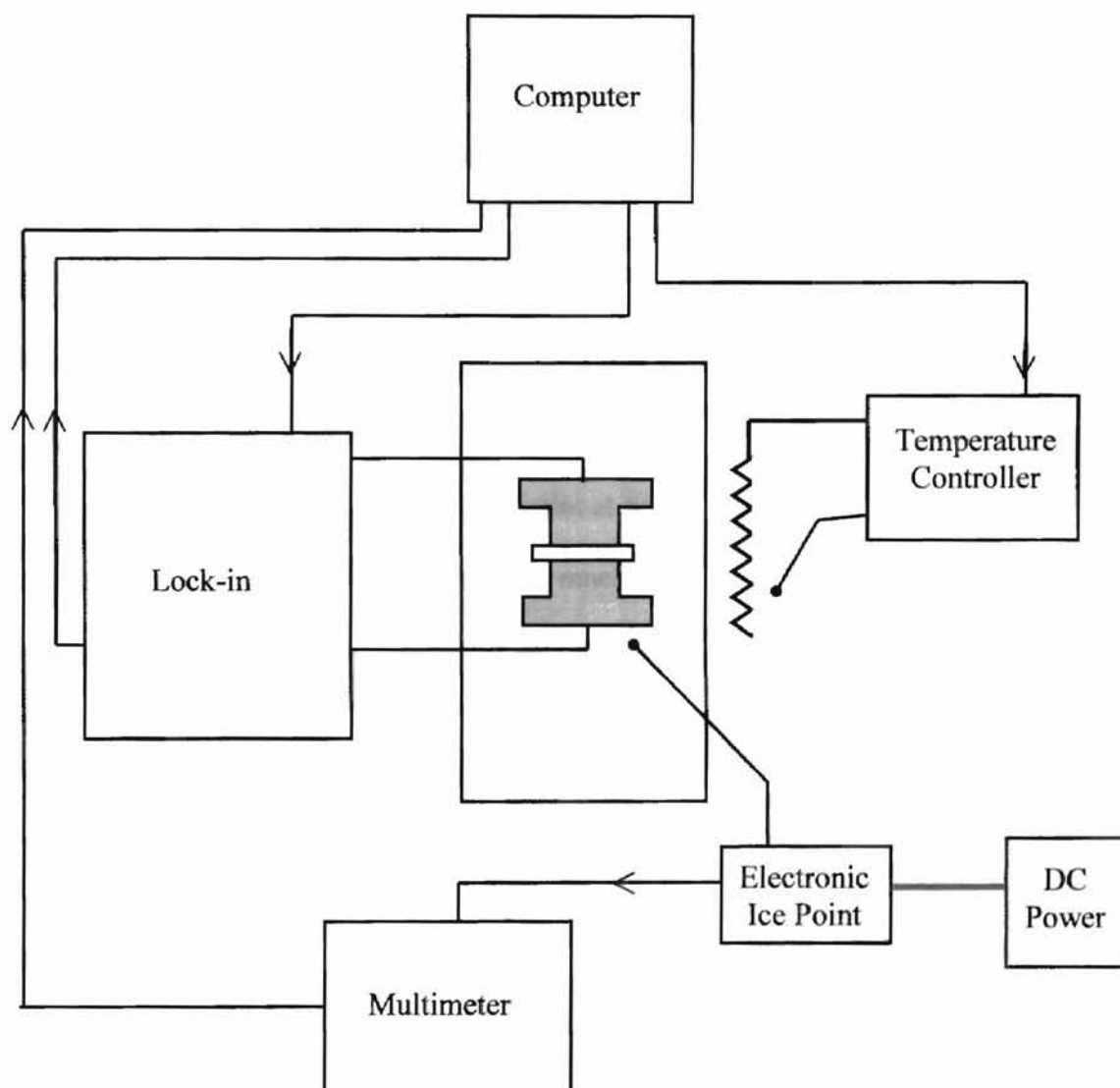
Procedure

The temperature of the coil was raised by the Omega controller in 4 degree increments, with 1½ hours given for the temperature inside to equilibrate. For each new temperature the real and imaginary components of the current were recorded at each frequency. The frequency was raised in 8% steps from the minimum to the maximum useful frequency. The complex current data, I, were transformed to complex

impedance data, Z, by the relationships $\quad Z'(\omega) = \dfrac{VI'(\omega)}{|I(\omega)|^2} \quad$ and $\quad Z''(\omega) = \dfrac{VI''(\omega)}{|I(\omega)|^2}$

which are easily derived from $\quad V = I\,Z$. The impedance data at each temperature were then plotted on a real vs. imaginary plane with the horizontal and vertical scale being equal. Figure 2.3 is an example of such a plot at several temperatures. Asymmetric CPE behavior such as this is seen to be very much the same in all of the samples. The point on the horizontal axis at which the impedance was almost purely resistive was then recorded to three significant figures. The resistance of the sample at each temperature was converted to conductivity by $\sigma = l/(AR)$ with units of $\Omega^{-1}\ cm^{-1}$. This data was then fit to an exponential decay curve of the form $y = a\ exp(-bx)$. Where x ($=1/kT$) and y ($=\sigma T$) were known parameters, while b ($=E_\sigma$) and a (pre-exponential factor) were to be determined by the best fit to the curve. The described fit was done using the points located in the conductivity range that displayed the most Arrhenius-like temperature dependence. At lower temperatures, a small deviation from Arrhenius temperature dependence was seen as well as at the highest temperatures, but the deviations are believed to be spurious, rather than indicating the onset of a different activation energy. For comparison between the different samples, the estimated margin of error in the

Figure 2.3 - Impedance plots of sample A2
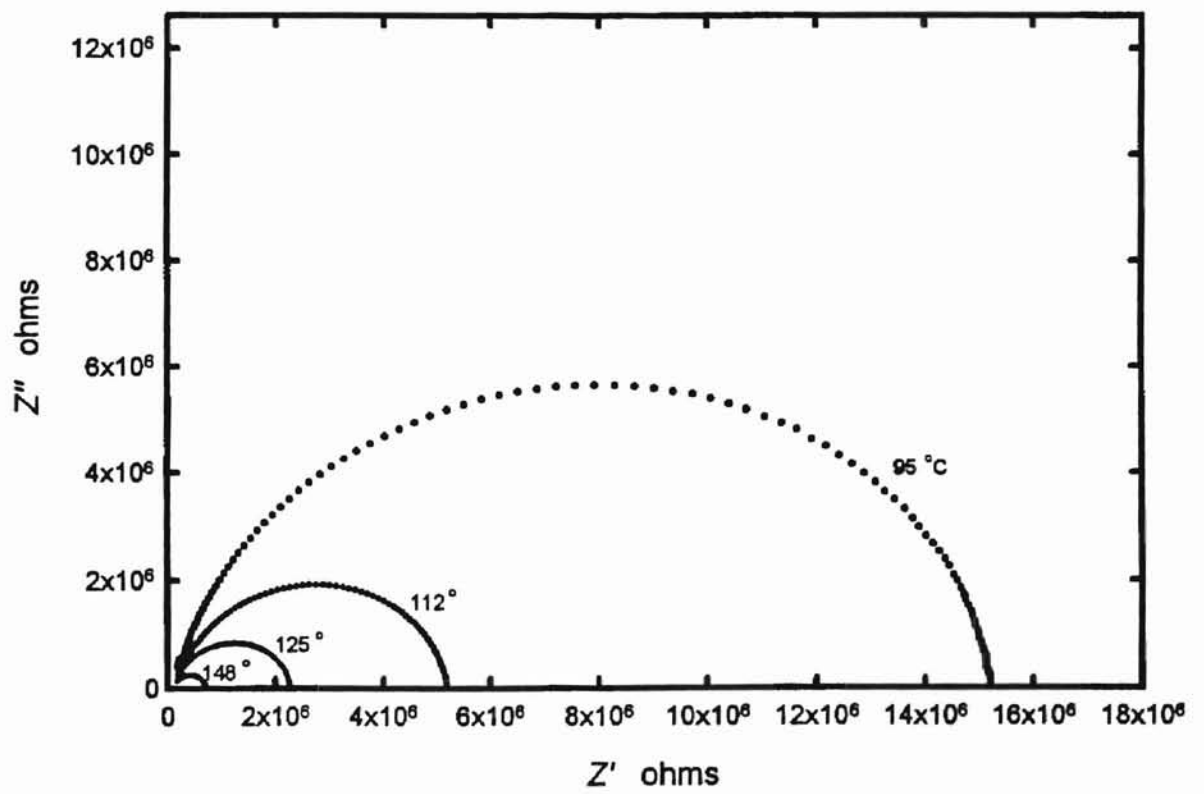
conductivity is $\pm$ 10% of the measured value.   The estimated margin of error in the

average activation energy is $\pm$ 0.5 % of the measured value.

CHAPTER III

RESULTS AND DISCUSSION

DC Conductivity

The Arrhenius plots of the 2.5 % europium samples are shown in figure 3.1. It is immediately apparent that the activation energy of each of these glasses is similar, however, table III reveals that there is a definite lowering of the activation energy with substitution of Al_2O_3. Figure 3.2 shows a plot of the change with a line added to emphasize the decreasing trend. This change in activation energy is responsible for the increase in conductivity seen in figure 3.3. An anomaly in this data is the close similarity between the 3 and 6 % Al_2O_3 samples. This will be discussed below. Figure 3.4 shows the pre-exponential factors derived from a fit to the Arrhenius equation.

In sodium aluminosilicate glass, the decrease in activation energy has long been understood to be due to the lower binding energy of those sodium ions that charge compensate the AlO_4 tetrahedra. Isard [25] showed that, with the exception of the first four percent, the addition of Al_2O_3 caused a decrease in activation energy until the number of Al^{3+} ions was equal to the number of Na^+ ions. Hsieh, et al. [10] used x-ray photoelectron spectroscopy (XPS) to show that the ionicity of the sodium increased with the addition of Al_2O_3. They also calculated that the strain energy increased with increasing Al_2O_3, but that this effect was small compared to the decrease of the binding energy [10]. The physical basis for the increase in activation energy with the initial four percent Al_2O_3 in simple sodium aluminosilicates has not been established, but it has been
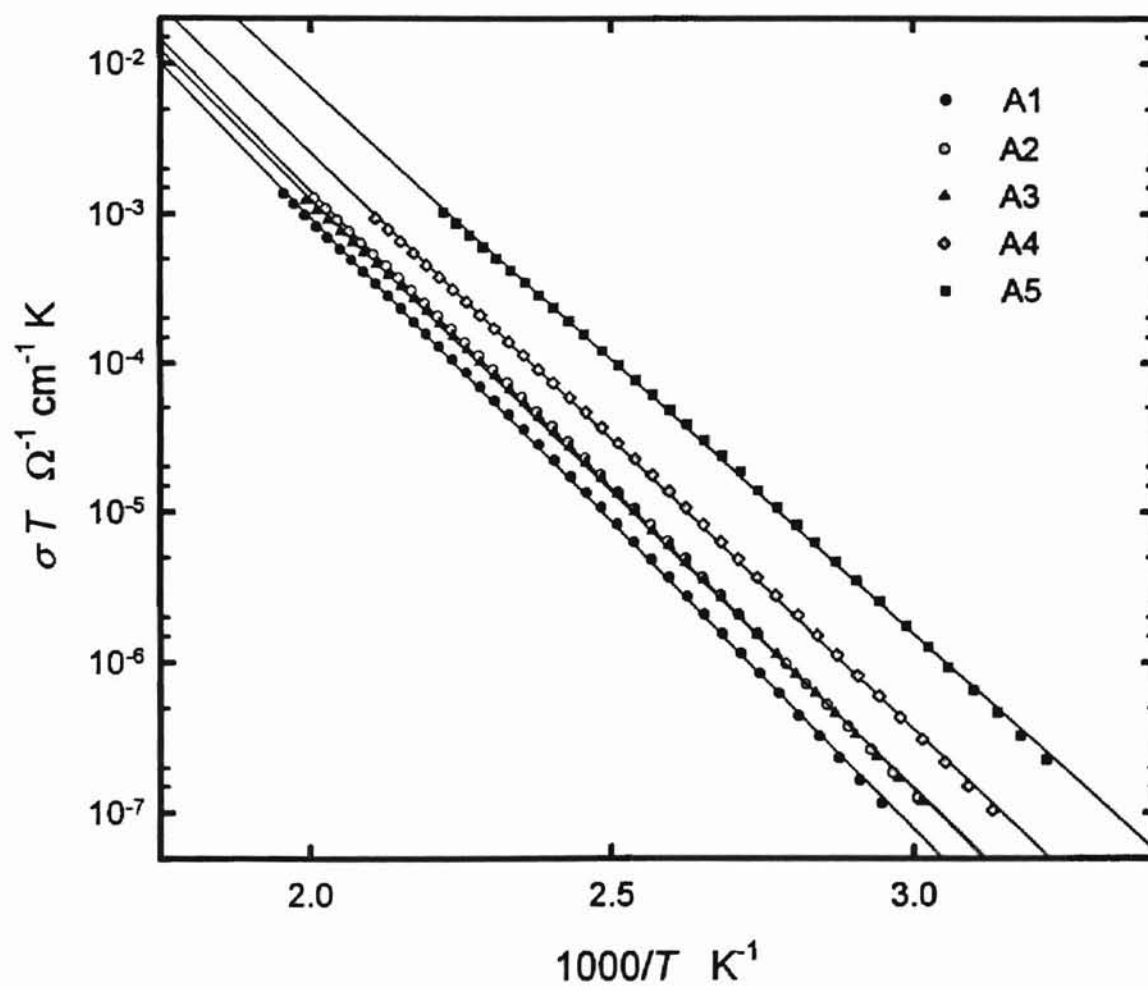
Figure 3.1 - 2.5 mol % Eu Arrhenius plots

Table III – Activation energy of Eu and Pr samples

Sample	E_a (eV)
A1	0.774
A2	0.758
A3	0.754
A4	0.732
A5	0.692
B1	0.775
B2	0.751
B3	0.726

Figure 3.2 - Activation energy vs. Al_2O_3 concentration in 2.5% Eu samples
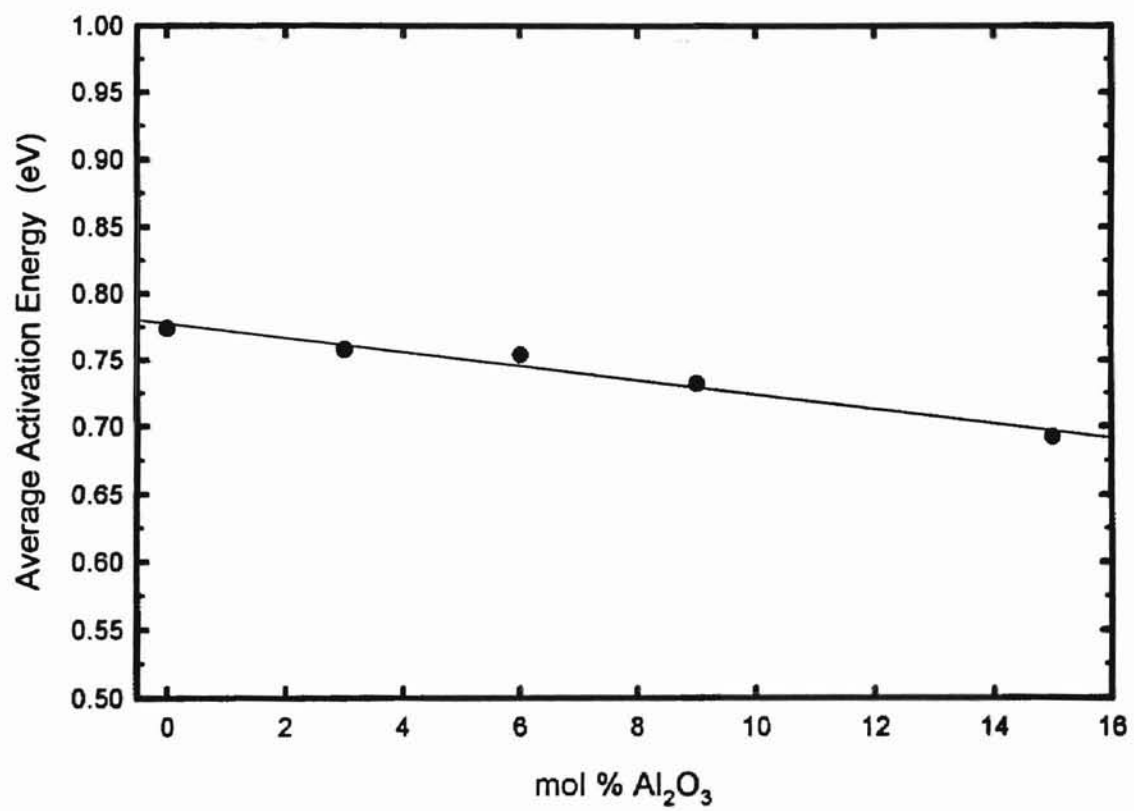
Figure 3.3 - Conductivity vs. Al_2O_3 concentration at 67 °C and 112 °C in 2.5 % Eu samples.
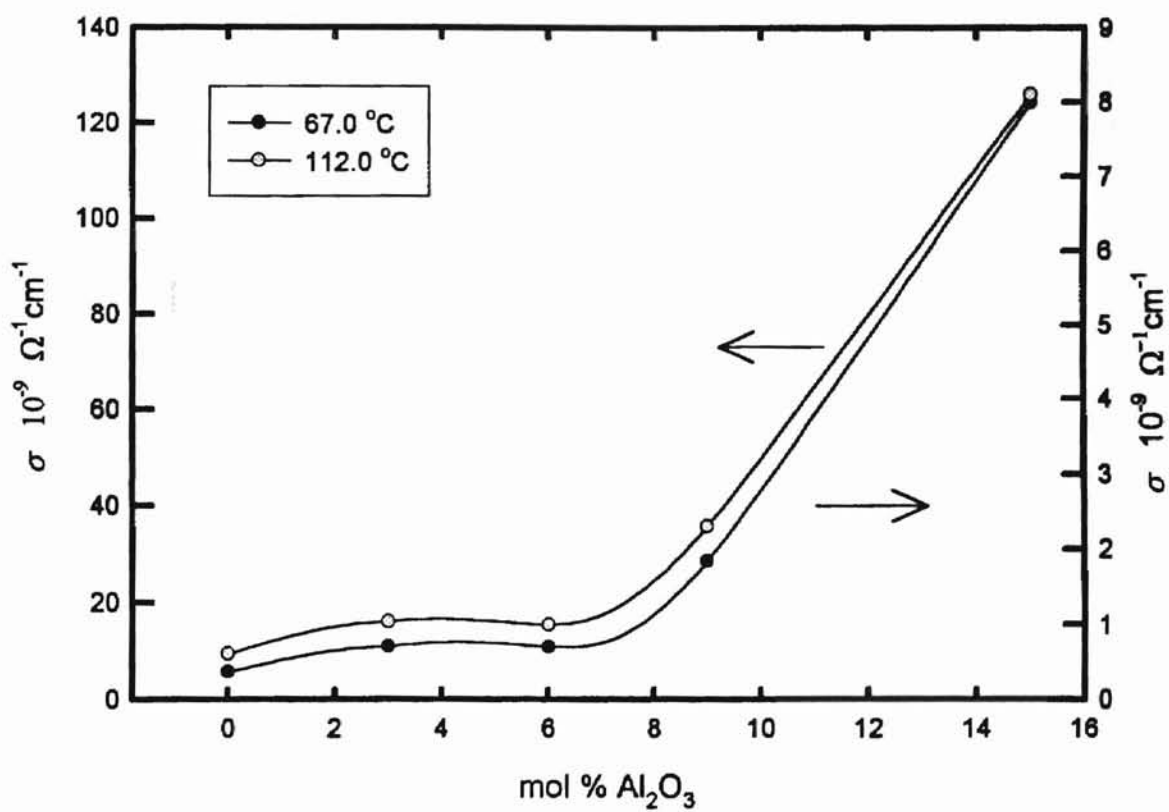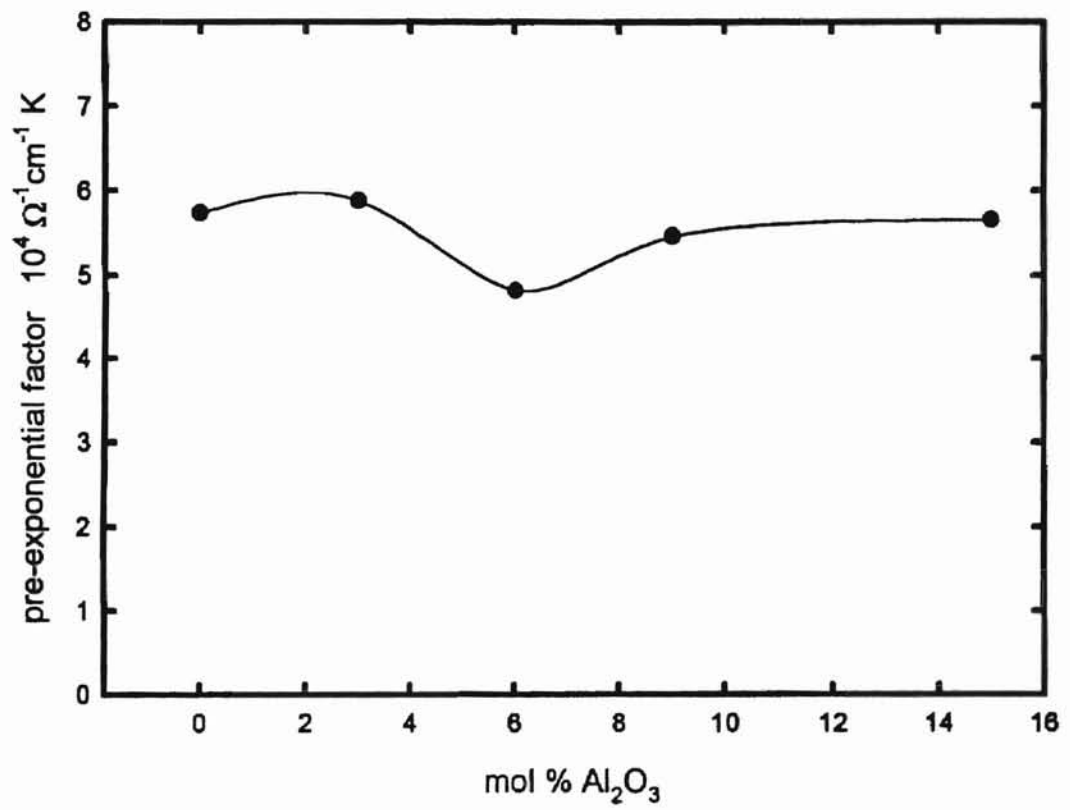
Figure 3.4 - Pre-exponential factor vs. Al_2O_3 concentration
in 2.5 % Eu samples

observed that the increase does not happen at all in the presence of a divalent modifier [26]. Moore and De Silva [27] found that the activation energy decreased with initial Al_2O_3 substitution in sodium calcium aluminosilicate glass. Their results are shown in table IV in terms of percent weight composition units and a constant, B, which is proportional to the activation energy. In the sample that corresponds closely to the 3 % Al_2O_3 samples in this thesis, the activation energy increased, but was still well below that of the original alumina-free sample. Moore and De Silva assigned no significance to this increase. Little other work has been done since to systematically investigate the effects of Al_2O_3 substitution on the ionic conductivity in alkali alkaline-earth aluminosilicate glass. Also, it has been shown that the addition of magnesium does not necessarily affect the conductivity of sodium silicate glass in the same way as calcium, although the presence of either causes a decrease in the conductivity [26]. Magnesium is probably the cause of the anomalous behavior seen in sample A3 of this research. The conductivity hardly increases between A2 and A3, and the activation energy only decreases slightly compared to the change between A1 and A2 as well as A3 and A4. Two additional samples of the same composition as A2 and A3 were made, and the same type of behavior was observed. An explanation for this behavior is now put forward as follows: In small concentrations, AlO_4 tetrahedra might be preferentially charge compensated by sodium rather than magnesium. Suppose that at 3 % Al_2O_3, each AlO_4 tetrahedron is charge compensated by a sodium ion; but that near 6 % Al_2O_3 and beyond, there is an equal distribution of the AlO_4 tetrahedra between the sodium and the magnesium ions. If this were the case, there would be a nearly equal number of loosely bound sodium ions in both the 3 and 6 % Al_2O_3 samples, and the number would increase with further Al_2O_3

Table IV – Activation energy as a function of low Al_2O_3
concentrations with 10 % wt. CaO and 16 % wt.
Na_2O (from ref. 25)

Weight % SiO_2	Weight % Al_2O_3	$B \times 10^{-3}$ ($\propto E_a$)
74	0	4.25
73	1	4.19
72	2	4.16
71	3	4.13
70	4	4.10
69	5	4.15

substitution. The pre-exponential factors are highly dependent on the conductivity range chosen for the fit and may not be accurate enough for one to assign significance to the trend in figure 3.4. However, it can be noted that the conductivity anomaly in sample A3 is observed in the pre-exponential factor as well as the activation energy.

Figure 3.5 shows the Arrhenius plots of the three praseodymium-doped samples. The conductivity of the 2.5 % praseodymium sample is seen in figure 3.6 to be less than that of the corresponding 2.5 % europium sample. This sample, B1, was the only one not made in the OSU crystal growth lab and should perhaps be given a greater margin of error to account for different thermal histories. The two samples with 0.5 % praseodymium are seen to be more conductive than either of the corresponding 2.5 % rare-earth samples.

Dielectric Properties

As was previously mentioned, dielectric properties are dependent on temperature as well as frequency. The dielectric properties presented here have all been measured at temperatures within two degrees of 67 °C. The dielectric constant, ε', of the 2.5 % Eu samples is plotted versus frequency in figure 3.7. The dielectric constant clearly increases with Al_2O_3 substitution. The corresponding plots for the praseodymium samples are shown in figure 3.8. At higher frequencies, the dielectric constant reflects more accurately the polarization taking place in the glass. Table IV gives the dielectric constant of all samples at 3000 Hz ($\omega \approx 19,000$ rad/s) and 5000 Hz ($\omega \approx 31,000$ rad/s). At these frequencies, the dielectric constant of sample B1 is equal to the dielectric

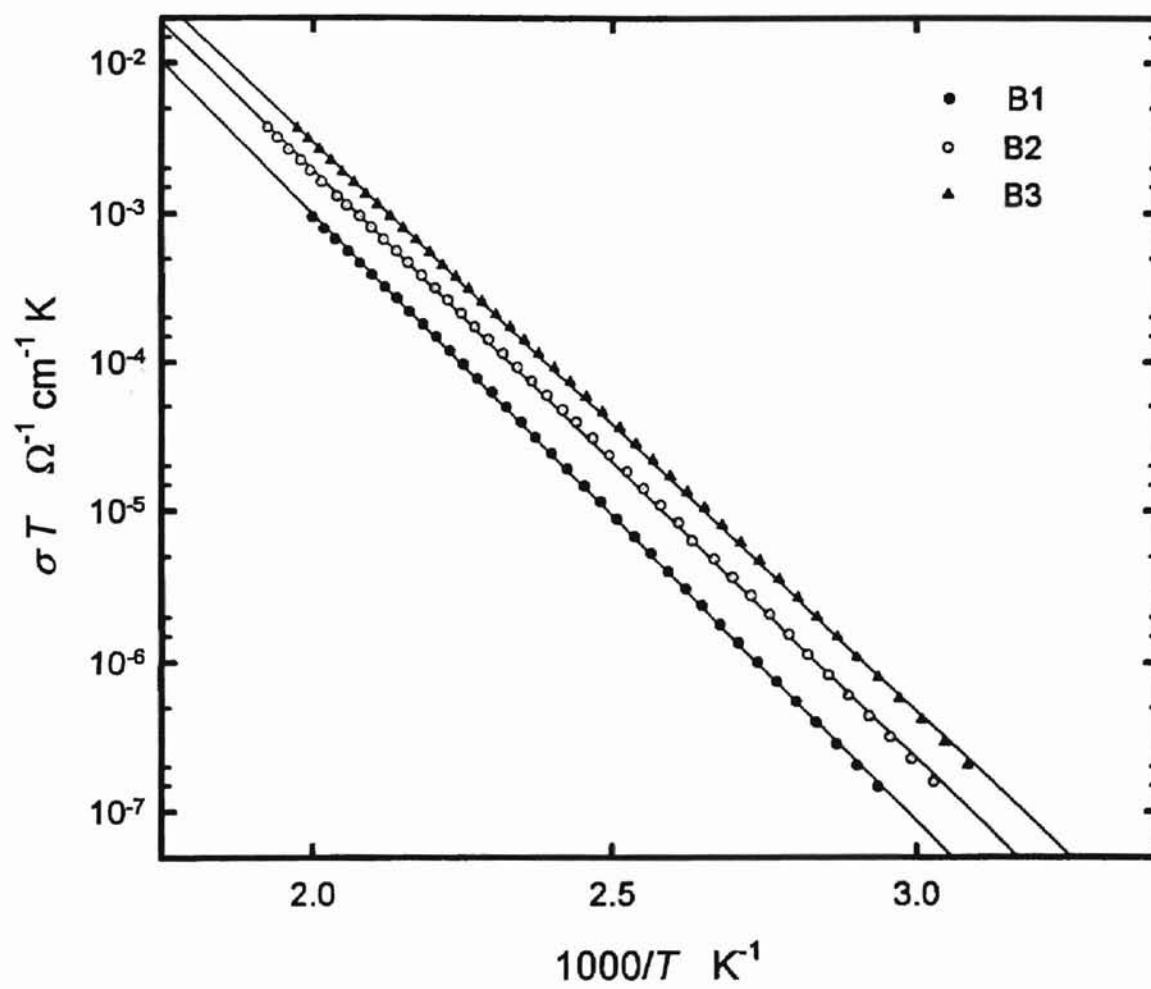Figure 3.5 - Arrhenius plots of Pr samples

Figure 3.6 - Conductivity vs. Al_2O_3 concentration at 112 $^{\circ}$C
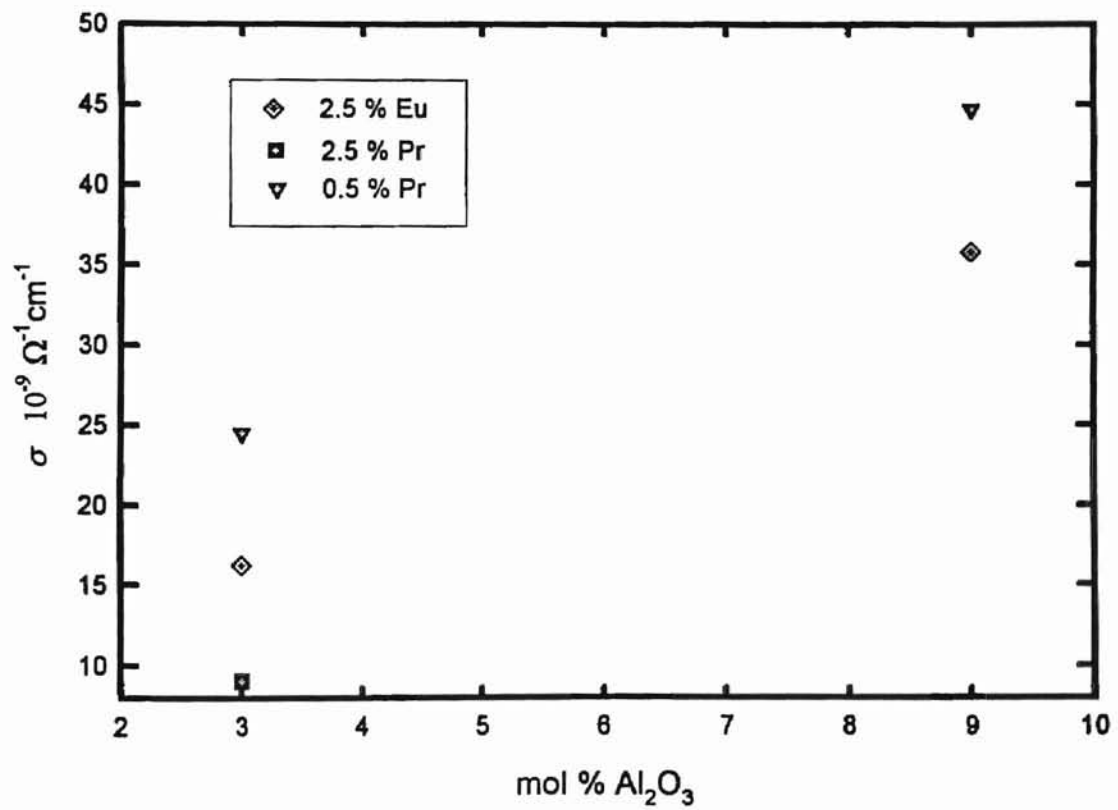in Pr samples and sample A2

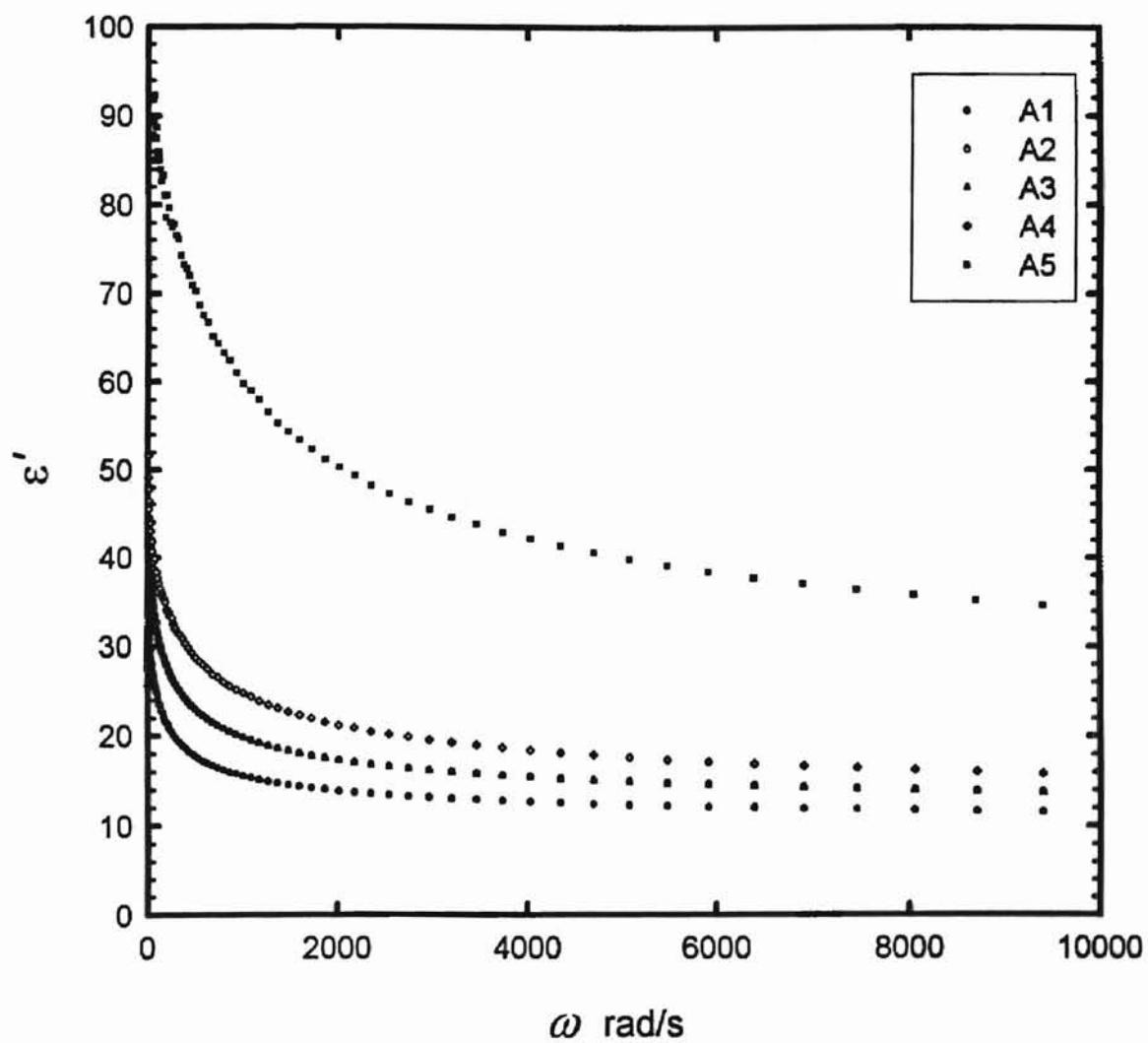Figure 3.7 - Dielectric constant vs. frequency at 67 °C
in 2.5% Eu samples

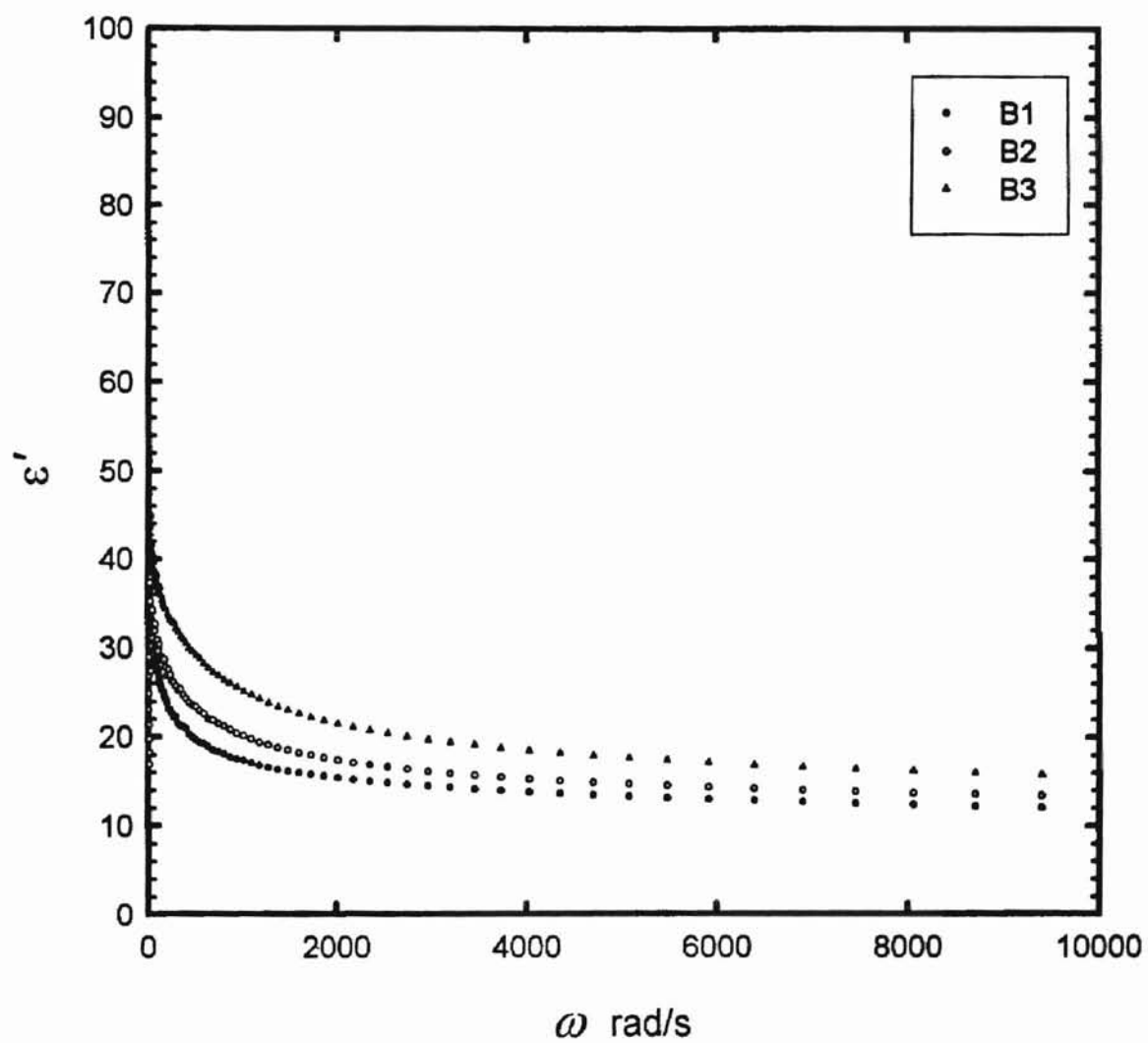Figure 3.8 - Dielectric constant vs. frequency at 67 °C in Pr samples

Table V – Dielectric constants at 67 °C for $v = 3000$ Hz and $v = 5000$ Hz

Sample	$\varepsilon'\ (\pm\,0.5)$ $v = 3000$ Hz	$\varepsilon'\ (\pm\,0.5)$ $v = 5000$ Hz
A1	11.0	10.7
A2	12.8	12.3
A3	12.7	12.2
A4	14.5	13.7
A5	31.7	29.2
B1	11.1	10.7
B2	12.1	11.6
B3	14.1	13.3

constant of sample A1. The dielectric constants of samples B2 and B3 are slightly less than or equal to those of samples A2 and A4 respectively.

The measured dielectric constants reflect both ionic and electronic polarization taking place in the glass. Hsieh, et al. [10] found an increase in the dielectric constant with increasing Al_2O_3 concentration in simple sodium aluminosilicate glass. They calculated that the ionic polarizability accounted for the increase while the electronic polarizability remained nearly constant. They attributed this increase in ionic polarizability to the increase in the ionicity of sodium with increasing Al_2O_3.

The dielectric loss angle, tan δ ($= \varepsilon''/\varepsilon'$), is plotted for the 2.5 % Eu samples in figure 3.9. It is found that while both ε' and ε'' is increasing with Al_2O_3, dielectric losses are getting disproportionately larger. On the same figure, the loss angle is plotted minus the DC conductivity contribution. This peak increases with Al_2O_3 concentration, becoming about 30 % greater in sample A5 than in sample A1 (not shown in figure 3.9 for clarity). However, when compared with the value for $\varepsilon''/\varepsilon'$ at the peak frequency, it is found that the ratio of relaxation losses to the total dielectric losses *at the peak relaxation frequency* does not show an increasing trend. This ratio, $(\varepsilon'' - \sigma_{dc}/\omega\varepsilon_0)/\varepsilon''$, is about equal to 0.37 at the peak relaxation frequency. Below that frequency, dielectric losses are dominated by long range conductivity and ε'' grows rapidly as frequency decreases. Loss plots of the praseodymium doped samples are shown in figure 3.10. The trend seems to be the same as in the europium doped samples, although the peaks are not as easily distinguished.

Finally, the imaginary modulus and impedance peaks of selected samples are shown in figures 3.11 – 3.16. The mean relaxation time, τ_0 (= $1/\omega_0$), is seen to decrease

Figure 3.9 - Dielectric losses vs. log(ω) at 67 °C in 2.5% Eu samples
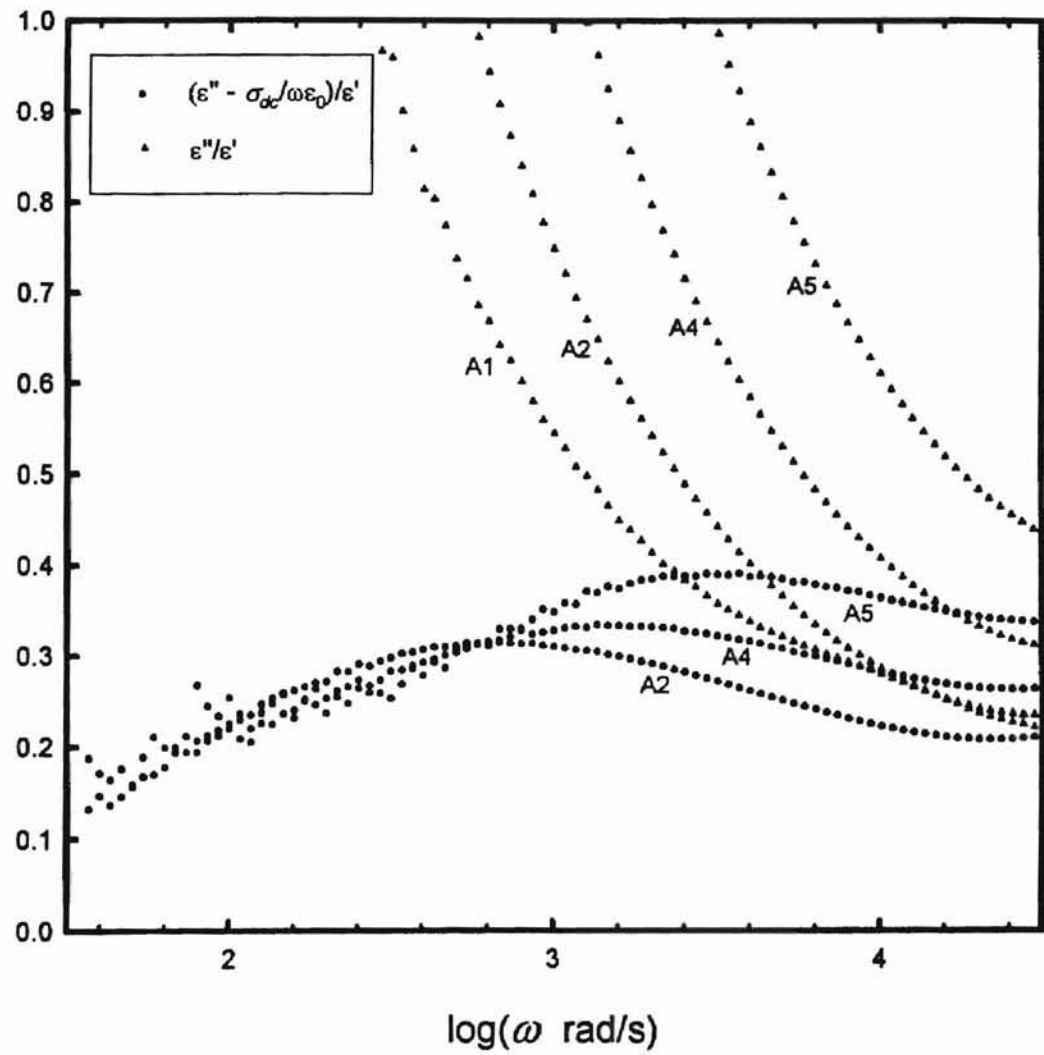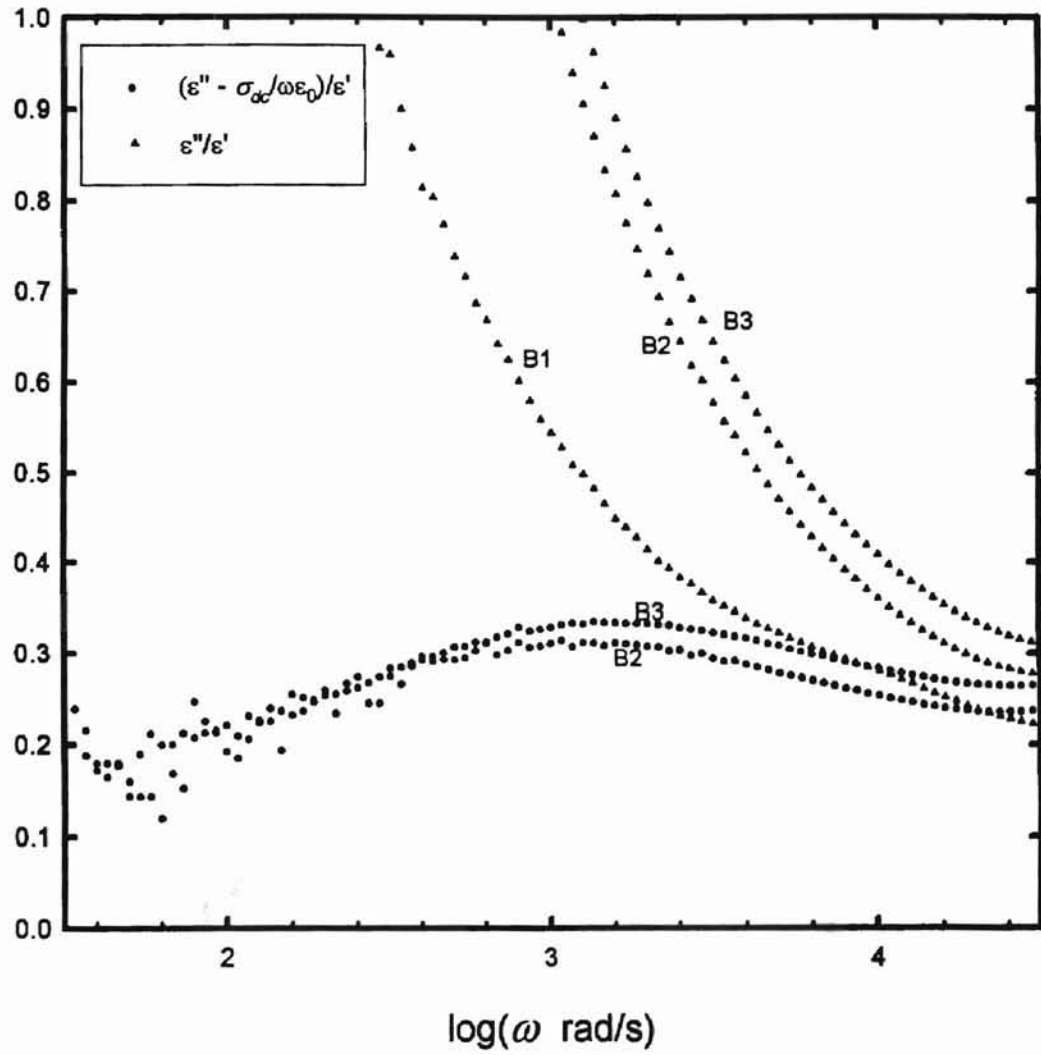
Figure 3.10 - Dielectric losses vs. $\log(\omega)$ at 67 $^{\circ}$C in Pr samples

$\log(\omega$ rad/s)

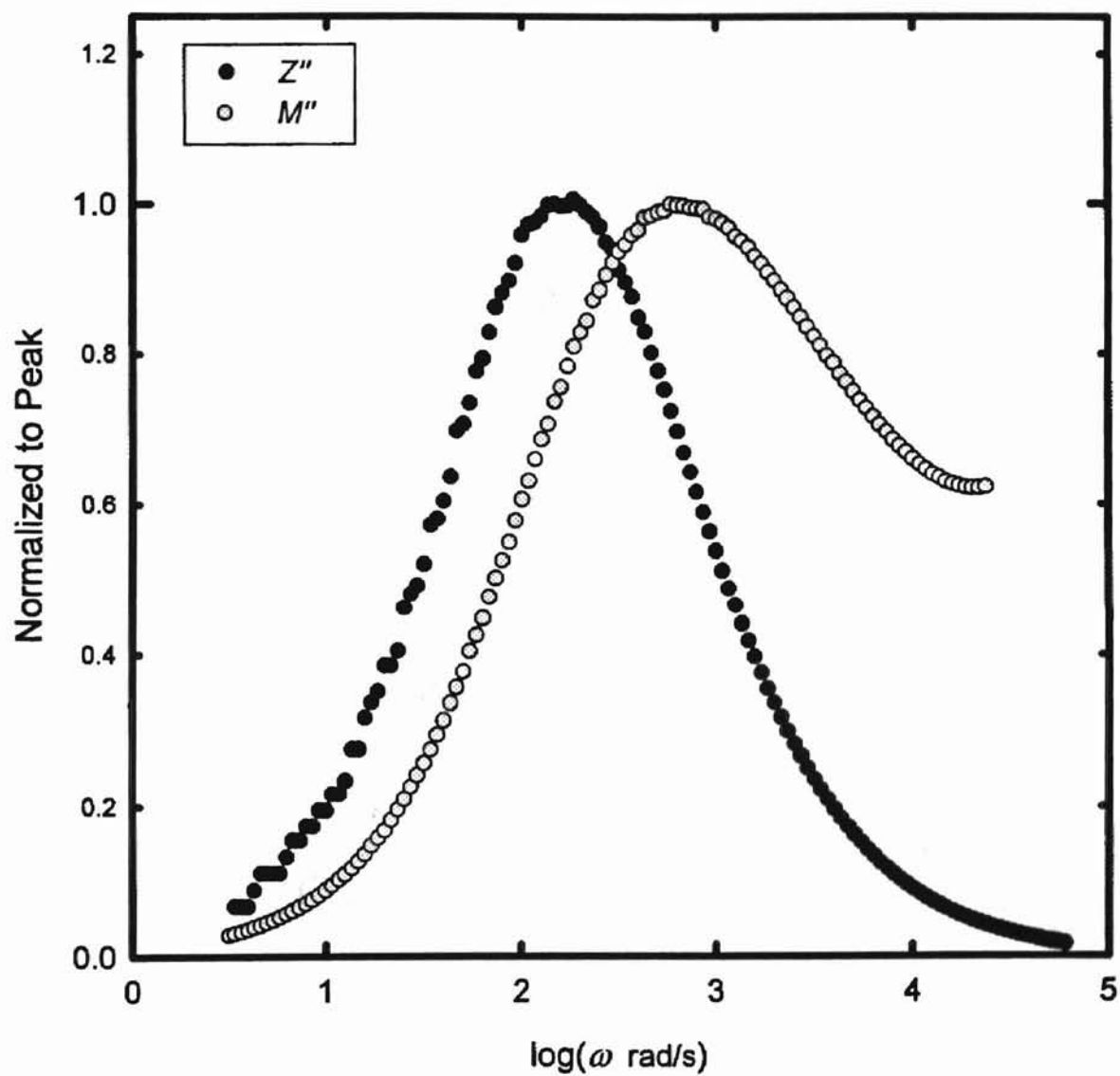Figure 3.11 - Normalized impedance and modulus peaks vs. log(ω) at 67 °C in sample A1

Figure 3.12 - Normalized impedance and modulus peaks vs. log(ω) at 67 °C in sample A2

Figure 3.13 - Normalized impedance and modulus peaks vs. log(ω) at 67 °C in sample A4
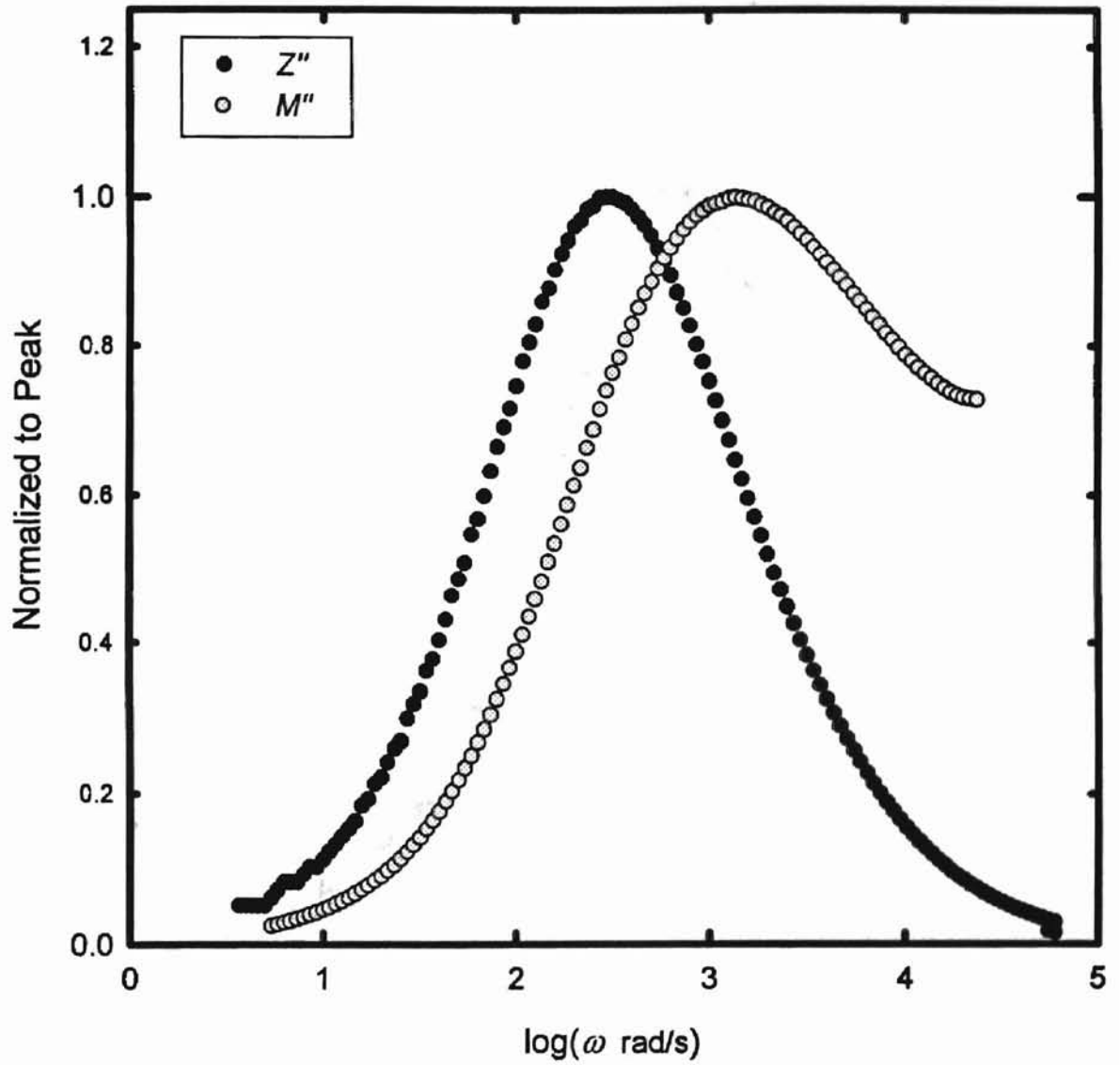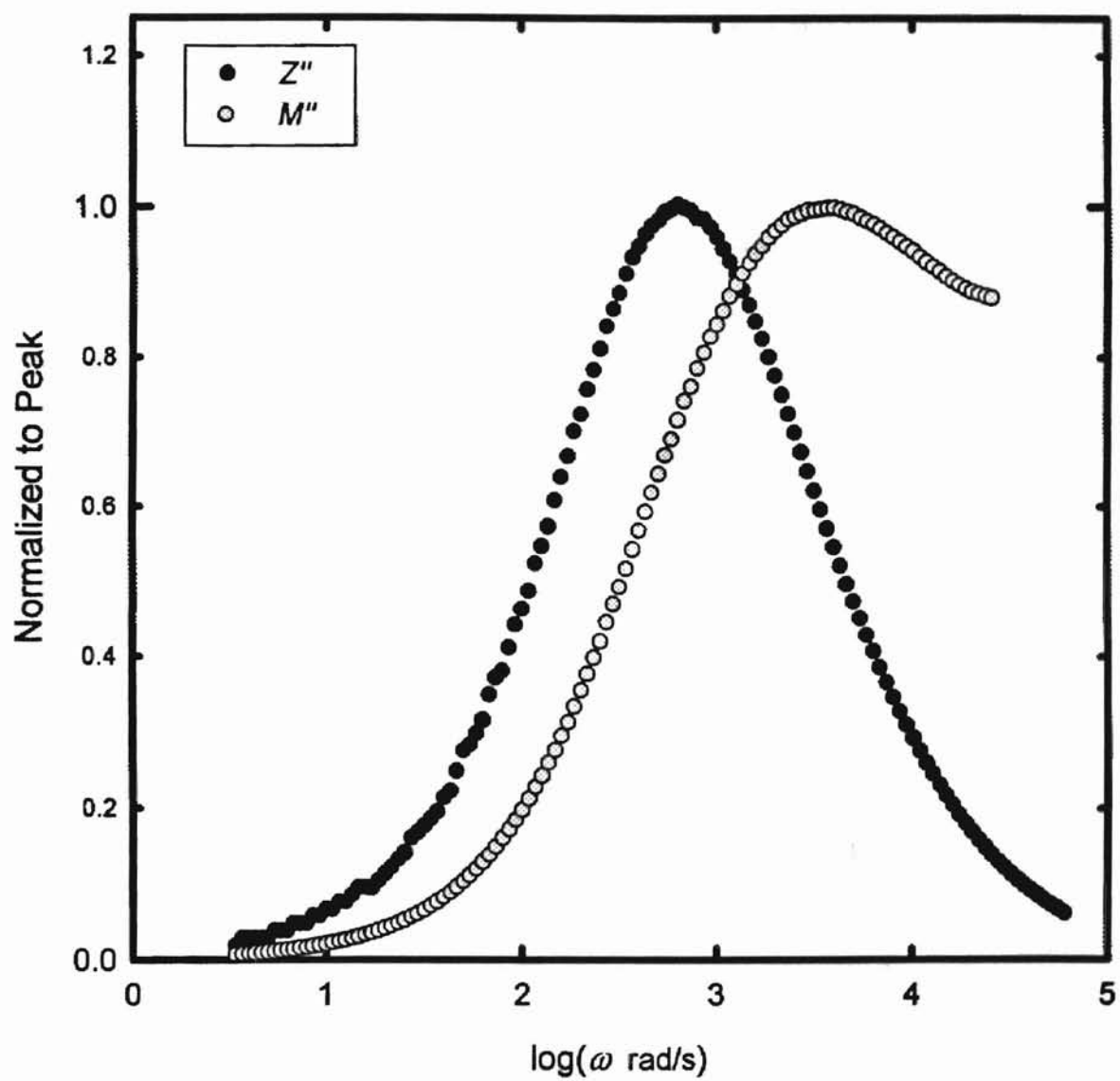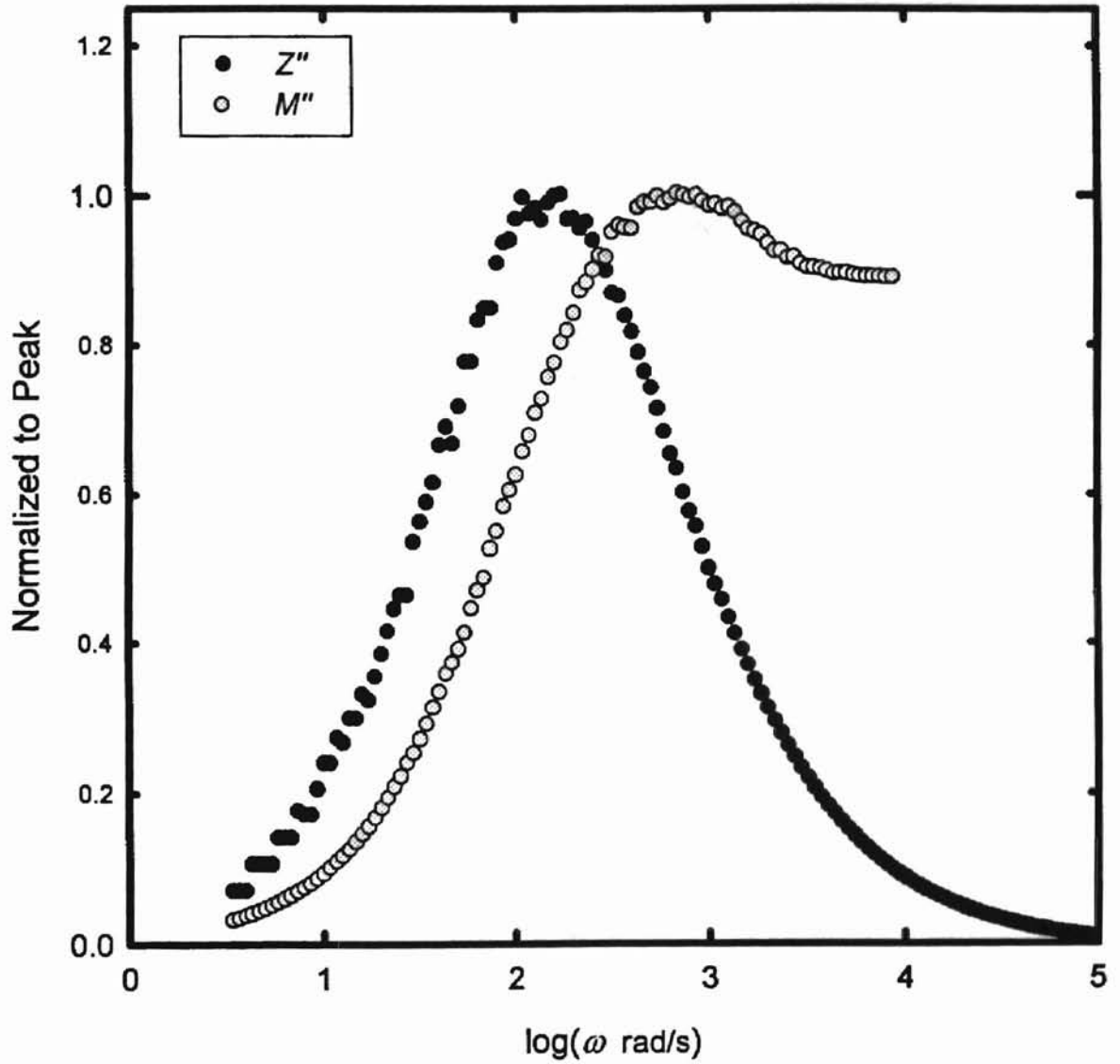
Figure 3.14 - Normalized impedance and modulus peaks vs. $\log(\omega)$ at 67 °C in sample B1

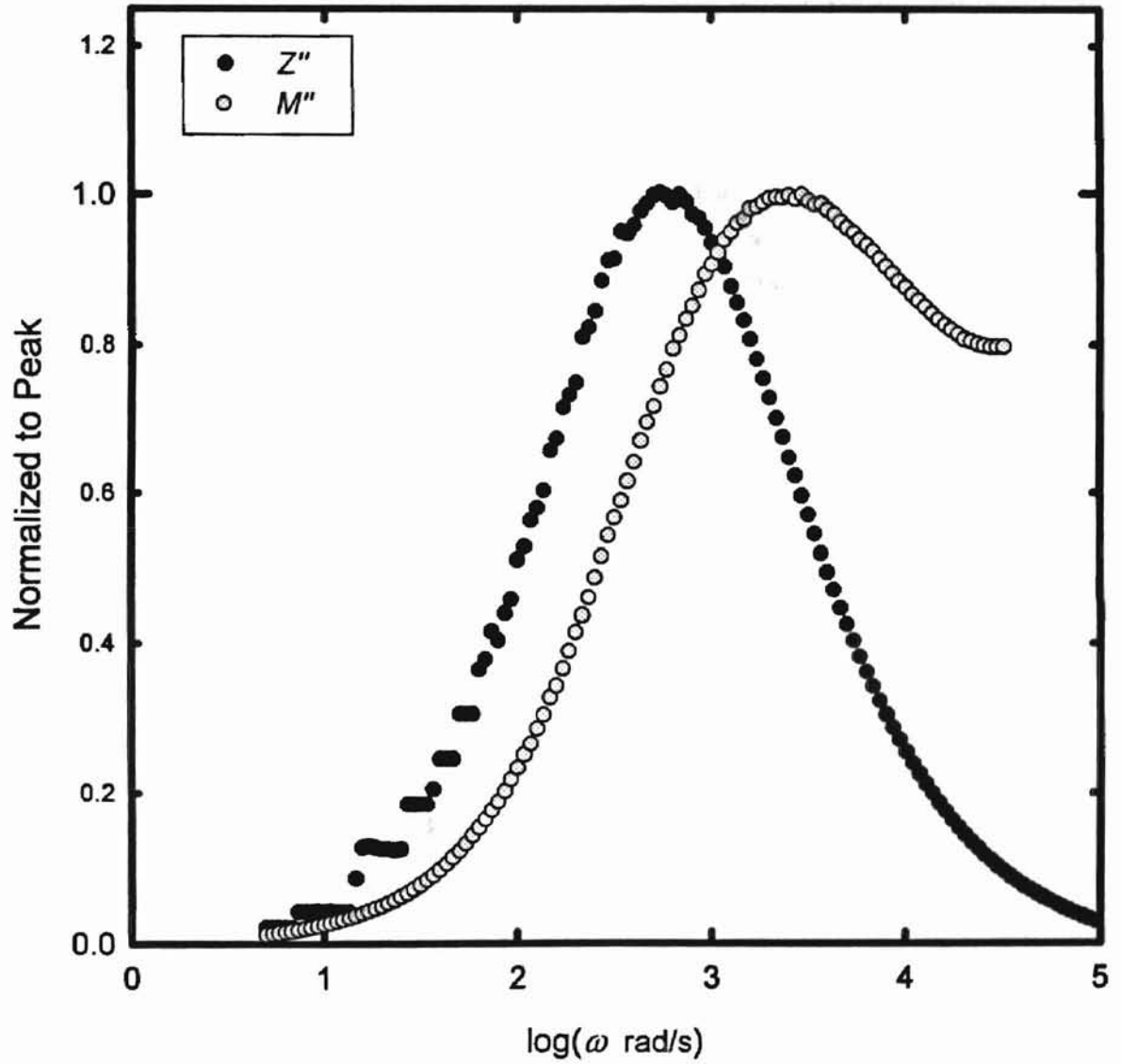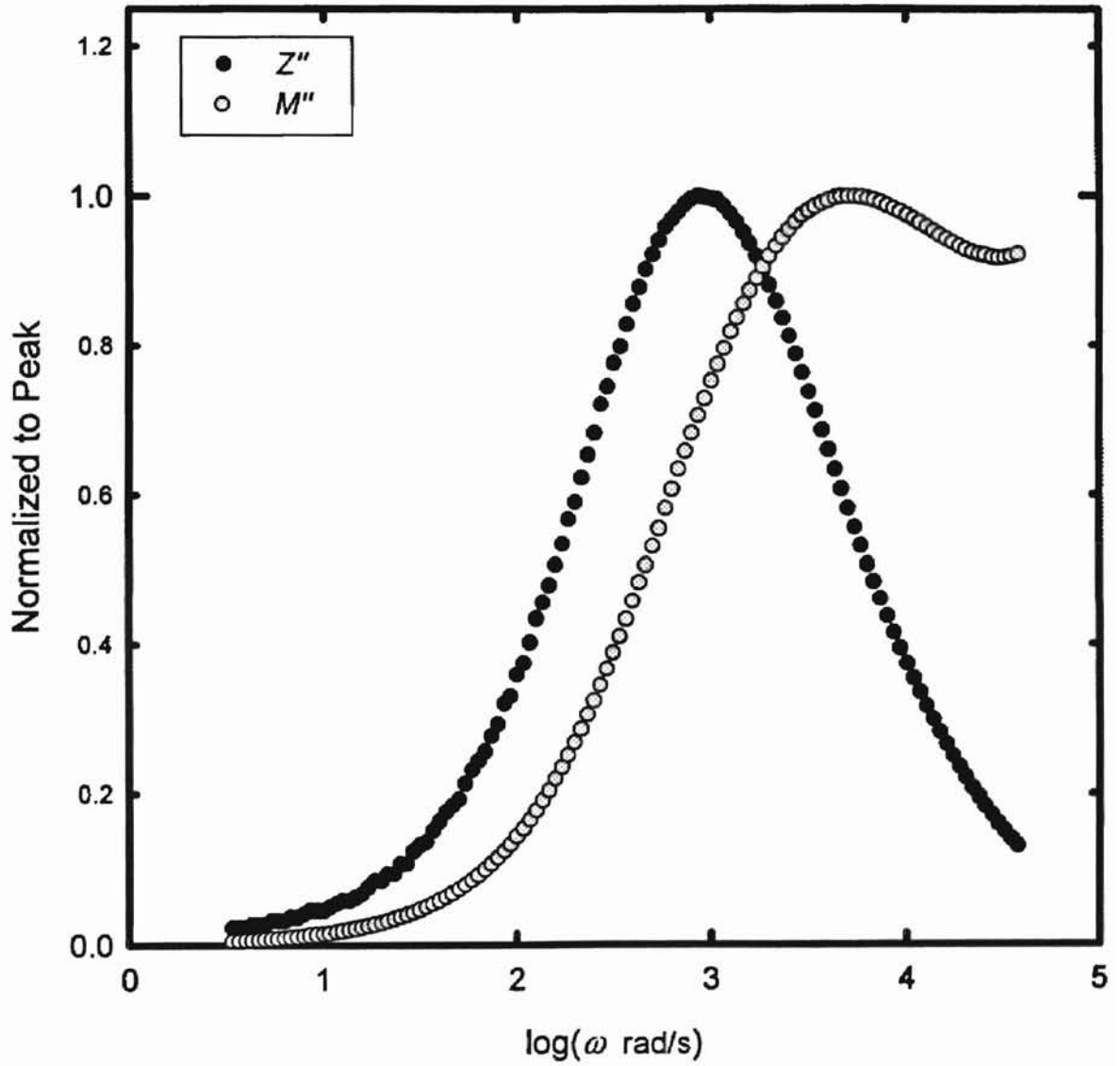Figure 3.15 - Normalized impedance and modulus peaks vs. log(ω) at 67 $^{\circ}$C in sample B2

Figure 3.16 - Normalized impedance and modulus peaks vs. $\log(\omega)$
at 67 $^{\circ}$C in sample B3

with increasing conductivity as is expected. The M'' peaks are nearly identical in shape to each other, as are the Z'' peaks (on the low frequency side). The separation of the two peaks can be indirectly related to the dielectric relaxation ratio ($r = \varepsilon_\infty/\varepsilon_s$) [18] and is seen to increase with Al_2O_3 concentration accordingly.

Comparison with Fourwave Mixing Experiments

It has been observed that the efficiency of the permanent laser-induced photorefractive index grating formation increases with the substitution of Al_2O_3 in the 2.5% Eu samples [25]. This change has been attributed to an increase in the number of loosely bound Na^+ ions as has been discussed in this thesis. The way in which the efficiency increases with Al_2O_3 concentration is quite different from the way in which the conductivity increases. In fact, the greatest increase in efficiency is seen between the samples A2 and A3, whereas it was shown in this thesis that the conductivity change between those two samples is minimal.

It was shown in this thesis that the activation energy of sample B1 is a little higher than that of sample A2. In the fourwave mixing experiments the grating growth was slower in sample B1 than in sample A2, but the total strength of the grating formed in sample B1 was higher. The rare-earth ion seems to have a blocking effect on the conduction of Na^+, as evidenced by the greater conductivity in samples B2 and B3. This blocking effect is likely to be present in the fourwave mixing experiments as well, but in those experiments, the rare-earth ion is known to also have an important role in the grating growth. Specifically, the rare-earth ion is excited by a laser and produces strong

vibration normal modes upon relaxation back to the ground state [28], giving Na^+ ions

the activation energy required for long-range migration.

CHAPTER IV

CONCLUSION

The ionic conductivity was measured for glasses of the composition $[(73-x)SiO_2-xAl_2O_3-12MgO-15Na_2O]_{.975}[Eu_2O_3]_{.025}$ where $x = 0, 3, 6, 9,$ and 15. Three praseodymium doped samples with varying Al_2O_3 and Pr_2O_3 concentrations were also studied. It was shown that the activation energy of the samples decreased with increasing concentration of Al_2O_3, resulting in an increase in conductivity. The changes were attributed to an increase in the number of loosely bonded Na^+ ions associated with network forming AlO_4 tetrahedra. The differences between the observed conductivity in these glasses and the known conductivity of simple sodium aluminosilicate glass were noted. The conductivity in the praseodymium doped samples increased when the amount of Pr_2O_3 was decreased to 0.5 %. The frequency dependence of the ionic conductivity was explored with plots of several impedance-related functions, including the complex dielectric constant and the electric modulus. The dielectric constant was shown to increase with Al_2O_3 concentration.

Finally, it was observed that there is not a simple correspondence between ionic conductivity and the efficiency of laser-induced photorefractive grating formation in these glasses, although the increase in the number of loosely bound Na^+ ions improves both processes.

REFERENCES

[1]   *Impedance Spectroscopy* edited by Macdonald, James R. (John Wiley & Sons, New York, 1987).

[2]   *Introduction to Glass Science and Technology* by Shelby, James E.(The Royal Society of Chemistry, Cambridge, 1997).

[3]   *Properties and Applications of Glass* by Rawson, Harold (Elsevier Scientific Publishing Company, New York, 1980).

[4]   *Glass Science* by Doremus, Robert H.(John Wiley and Sons, New York, 1994).

[5]   F.M. Durville, E.G. Behrens, and R.C. Powell, Phys. Rev. B **34**, 4213 (1986)

[6]   *Materials Science and Technology: A Comprehensive Treatment* Vol. 9 edited by Cahn R.W., Haasen P., and Kramer E.J. (VCH, New York, 1996).

[7]   *Electrical Conductivity in Ceramics and Glass* edited by Tallan, Norman M. (Marcel Dekker, New York, 1974).

[8]   *Treatise on Materials Science and Technology* Vol. 12 edited by Tomozawa, Minoru and Doremus, Robert H. (Academic Press, New York, 1977).

[9]   M.L. Meade, J. Phys. E **15**, 395 (1982)

[10]   C.H. Hsieh, H. Jain, and E.I. Kamitsos, J. Appl. Phys. **80**, 1704 (1996)

[11]   C.H. Hsieh and H. Jain, J. Non-Cryst. Solids **183**, 1 (1995)

[12]   *Chemical Approach to Glass* by Volf, M.B. (Elsevier, New York, 1984).

[13]   N. Evans, Advanced Materials and Processes **140**, No. 5, 41 (1991)

[14]   *An Introduction to Electrical Instrumentation and Measurement Systems* by Gregory, B.A. (John Wiley and Sons, New York, 1981).

[15]   *Model SR830 DSP Lock-In Amplifier Technical Manual* (Stanford Research Systems, Inc., Sunnyvale, 1993).

[16]   G. Chiodelli and P. Lupotto, J. Electrochem. Soc. **138**, 2703 (1991).

[17]   J.C. Wang, Electrochimica Acta **38**, 2111 (1993)

[18]   R. Gerhardt, J. Phys. Chem. Solids **55**, 1491 (1994)

[19] S.R. Elliott, J. Non-Cryst. Solids **170**, 97 (1994)

[20] J.M. Stevels, *Encyclopedia of Physics*, Vol. 20, 350 (Springer Verlag, Berlin, 1957)

[21] *Electronic Instrument Handbook* edited by Coombs, Clyde F. Jr. (McGraw-Hill, Inc., US, 1994).

[22] *Progress in Ceramic Science*, Vol. 3 by Owen, A.E. , edited by Burke, J.E. (Pergamon, London, 1963)

[23] J.O. Isard, J. Soc. Glass Techn. **43**, 113 (1959)

[24] *Introduction to the Physical Chemistry of the Vitreous State* by Balta E. and Balta P. (Abacus Press, Romania, 1976).

[25] A.Y. Hamad, unpublished work.

[26] *The Structure of Glass*, Vol. 4 edited by Mazurin, O.V. (Consultants Bureau, New York, 1965)

[27] H. Moore and R.C. De Silva, J. Soc. Glass Tech. **36**, 5 (1952)

[28] G.S. Dixon, A.Y. Hamad, and J.P. Wicksted, Phys. Rev. B **58**, 200 (1998)

[29] Z. Utegulov, Master's Thesis, Oklahoma State University (1999)

VITA 2

Michael Hogsed

Candidate for the Degree of

Master of Science

Thesis: IONIC CONDUCTIVITY IN RARE-EARTH DOPED
          ALUMINOSILICATE GLASSES.

Major Field: Physics

Biographical:

> Personal Data: Born in Canton, Ohio on August 19, 1973, the son of Dr. James
> and Barbra Hogsed.

> Education: Graduated from San Antonio Christian School, San Antonio, Texas in
> May, 1992; received Bachelor of Science degree in Physics from Baylor University,
> Waco, Texas in May, 1997. Completed the requirements for the Master of Science
> degree with a major in Physics at Oklahoma State University in May, 1999.

> Professional Experience: Employed as a graduate teaching assistant; Oklahoma
> State University, 1997-1998. Employed as a graduate research assistant; Oklahoma
> State University, 1998-present.